

Uncovering the Ediacaran phosphorus cycle

<https://doi.org/10.1038/s41586-023-06077-6>

Received: 7 December 2022

Accepted: 12 April 2023

Published online: 31 May 2023

 Check for updates

Matthew S. Dodd^{1,2,3,4,5}, Wei Shi^{1,3}, Chao Li^{1,2,3}, Zihu Zhang^{1,3}, Meng Cheng^{1,3}, Haodong Gu², Dalton S. Hardisty⁶, Sean J. Loyd⁷, Malcolm W. Wallace⁸, Ashleigh V.S. Hood⁸, Kelsey Lamothe⁸, Benjamin J. W. Mills⁹, Simon W. Poulton⁹ & Timothy W. Lyons¹⁰

Phosphorus is a limiting nutrient that is thought to control oceanic oxygen levels to a large extent^{1–3}. A possible increase in marine phosphorus concentrations during the Ediacaran Period (about 635–539 million years ago) has been proposed as a driver for increasing oxygen levels^{4–6}. However, little is known about the nature and evolution of phosphorus cycling during this time⁴. Here we use carbonate-associated phosphate (CAP) from six globally distributed sections to reconstruct oceanic phosphorus concentrations during a large negative carbon-isotope excursion—the Shuram excursion (SE)—which co-occurred with global oceanic oxygenation^{7–9}. Our data suggest pulsed increases in oceanic phosphorus concentrations during the falling and rising limbs of the SE. Using a quantitative biogeochemical model, we propose that this observation could be explained by carbon dioxide and phosphorus release from marine organic-matter oxidation primarily by sulfate, with further phosphorus release from carbon-dioxide-driven weathering on land. Collectively, this may have resulted in elevated organic-pyrite burial and ocean oxygenation. Our CAP data also seem to suggest equivalent oceanic phosphorus concentrations under maximum and minimum extents of ocean anoxia across the SE. This observation may reflect decoupled phosphorus and ocean anoxia cycles, as opposed to their coupled nature in the modern ocean. Our findings point to external stimuli such as sulfate weathering rather than internal oceanic phosphorus–oxygen cycling alone as a possible control on oceanic oxygenation in the Ediacaran. In turn, this may help explain the prolonged rise of atmospheric oxygen levels.

Phosphorus (P) is considered the primary limiting nutrient for marine productivity on geological timescales¹. Consequently, it has been proposed that the coupled cycling of P and oxygen (O_2) maintains O_2 availability over million-year timescales, preventing runaway ocean anoxia in the Phanerozoic (<539 million years ago (Ma))^{1–3} and thereby sustaining oxygen-demanding eukaryotic life. This relationship exists because dissolved P and O_2 follow negative feedback cycles, in which higher oceanic P concentrations under ocean anoxia enhance photosynthetic production of oxygen, which oxygenates previously anoxic water masses^{1,2}. This feedback arises because of the release of P from both the decomposition of organic matter and iron (Fe) (oxyhydr)oxides in anoxic sediments¹⁰. Under oxygenated bottom waters, this released P generally becomes trapped in the sediment by a variety of pathways, including uptake by Fe (oxyhydr)oxides, biological sequestration of polyphosphates^{2,10} or formation of authigenic phosphate minerals, all of which prevent the return of P to the oceans¹⁰. Under anoxic bottom waters, a proportion of the mobilized P can diffuse out of the sediment¹¹. However, enhanced organic-matter preservation¹¹ and iron-mineral formation under ferruginous (anoxic and Fe^{2+} -containing) conditions¹² can aid P retention in the sediments. Consequently, euxinic

conditions (anoxic and sulfidic) are particularly conducive to sedimentary P release because of uptake of dissolved iron as sulfide minerals, thereby limiting P sequestration by iron minerals¹².

The coupled cycling of P and O_2 may have supported high levels of ocean P in the largely anoxic Precambrian oceans (>539 Ma)¹³, as interpreted from P/Fe ratios in iron formations¹⁴. Conversely, alternative interpretations of this P/Fe record suggest low oceanic P (refs. 15,16), owing to effective drawdown of P by iron minerals and sequestration under ferruginous conditions^{15,17}. Alternatively, low-P Precambrian oceans may have arisen because of a lack of oxidants, such as O_2 and sulfate, which suppressed P release from organic matter^{4,5}. Some researchers have speculated that these low marine P levels substantially increased during the Ediacaran in conjunction with extensive deep-ocean oxygenation, giving rise to modern-like oceanic P levels^{4–6}. The Ediacaran P cycle is thus key to any understanding of how the interaction of P and O_2 cycles evolved from the Precambrian to the modern world and its potential role in the coevolution of atmospheric O_2 and complex life. However, little is known about the nature and evolution of the Ediacaran P cycle. To shed light on the Ediacaran P cycle, we use the newly developed CAP proxy to directly document

¹State Key Laboratory of Oil and Gas Reservoir Geology and Exploitation, Institute of Sedimentary Geology, Chengdu University of Technology, Chengdu, China. ²State Key Laboratory of Biogeology and Environmental Geology, China University of Geosciences, Wuhan, China. ³International Center for Sedimentary Geochemistry and Biogeochemistry Research, Chengdu University of Technology, Chengdu, China. ⁴School of Earth Sciences, University of Western Australia, Perth, Western Australia, Australia. ⁵Forrest Research Foundation, Perth, Western Australia, Australia. ⁶Department of Earth and Environmental Sciences, Michigan State University, East Lansing, MI, USA. ⁷Department of Geological Sciences, California State University, Fullerton, CA, USA. ⁸School of Geography, Earth and Atmospheric Sciences, University of Melbourne, Parkville, Victoria, Australia. ⁹School of Earth and Environment, University of Leeds, Leeds, UK. ¹⁰Department of Earth and Planetary Sciences, University of California, Riverside, Riverside, CA, USA. ¹¹e-mail: chao.li@cdut.edu.cn

variability in oceanic P concentrations during a notable Ediacaran ocean-oxygenation event^{7–9,18}. This episode witnessed considerable diversification of multicellular eukaryotic and metazoan life^{18,19} and the largest known negative carbonate carbon-isotope ($\delta^{13}\text{C}_{\text{carb}}$) excursion in Earth's history, referred to here as the SE.

We analysed six globally distributed and well-preserved carbonate sections (Fig. 1a; see Methods) to capture oceanic P variability during the SE: the Jiulongwan and Sishang sections of the Doushantuo and Dengying formations from South China, the Mochia-Khutuk section of the Shuiquan Formation in Northwest China, the Cerro Rajón section of the Clemente, Pitiquito and Gamuza formations of northern Mexico, the Death Valley section of the Johnnie Formation of southwestern USA and the Parachilna Gorge section of the Wonoka Formation of South Australia. All sections preserve >10‰ shifts in $\delta^{13}\text{C}_{\text{carb}}$ values characteristic of the SE^{20–27} (Fig. 1b–g). The six sections reported here are taken to represent global expressions of the SE and are temporally correlated through a combination of chemostratigraphy, fossil assemblages, lithological correlation and palaeomagnetism (see Supplementary Information 2).

Among all the measured sections, CAP shows a similar 'M-shaped' pattern, which is broadly coincident with four stages in the temporal evolution of the $\delta^{13}\text{C}_{\text{carb}}$ trend at each section (stages I–IV; Fig. 1b–g). Note that the Death Valley and Parachilna Gorge sections do not preserve the final recovery and initial drop in $\delta^{13}\text{C}_{\text{carb}}$ of the SE, respectively, and the Sishang section is faulted in the middle (Fig. 1d,e,g); however, the sections capture three out of the four CAP shifts identified in other global sections. In stage I (falling limb of the SE), there is a large increase in CAP ('P-1st' in Fig. 1) at the onset of declining $\delta^{13}\text{C}_{\text{carb}}$ values, with CAP values reaching between 0.39 and 1.33 mmol mol⁻¹ (CAP/(Ca+Mg)). This increase is followed by an equally large decrease in CAP to a minimum during the mid-SE (stage II; the plateau in SE $\delta^{13}\text{C}_{\text{carb}}$ values), with CAP values ranging between 0.03 and 0.24 mmol mol⁻¹. A rebound in CAP begins in the mid-SE (stage II) and continues to increase as $\delta^{13}\text{C}_{\text{carb}}$ values increase towards the termination of the SE, reaching values of 0.32–2.18 mmol mol⁻¹ (stage III; rising limb of the SE; 'P-2nd' in Fig. 1), which is then followed by a gradual decline in CAP values to between 0.07 and 0.20 mmol mol⁻¹ following the termination of the SE (stage IV; a return to pre-SE $\delta^{13}\text{C}_{\text{carb}}$ values). Given that the CAP trends in all sections are connected to the $\delta^{13}\text{C}_{\text{carb}}$ excursion, and because the SE is approximately synchronous globally²⁸, a broadly contemporaneous shift in global oceanic P levels is implied.

CAP can be used to produce direct estimates of relative changes in palaeoceanic P levels at the time of carbonate precipitation, if contamination, diagenetic alteration and other potential changes in oceanic chemistry can be evaluated²⁹. Our CAP extractions show no signs of contamination by other sources of sedimentary P, as there is little to no correlation between CAP and bulk-rock P, total organic carbon (TOC) or La (an element used for tracking phosphate mineral dissolution^{29,30}) (Extended Data Table 1; see Supplementary Information 3). Encouragingly, an independent methodology using *in situ* analysis of CAP in carbonate-preserving primary textures gives trends consistent with our bulk CAP data from the Dengying Formation in the Jiulongwan section of South China³⁰ (Fig. 1b).

Although the global occurrence of our CAP trends is difficult to reconcile with diagenetic alteration, globally synchronized diagenetic alteration of carbonate has been purported to result after marine regression exposes platforms to meteoric waters³¹. The SE, however, is recognized as a marine transgression event, which is unlikely to expose carbonate sediments to meteoric alteration³². Nevertheless, to assess the potential effects of diagenetic alteration on CAP, we use an open-system diagenetic model to evaluate chemical signals of alteration (Extended Data Fig. 1). Our diagenetic model shows that CAP is altered at similar or greater fluid-to-rock ratios than several carbonate proxies, such as $\delta^{13}\text{C}_{\text{carb}}$, $\delta^{18}\text{O}$, $\delta^{44/40}\text{Ca}$ or Mn/Sr. Therefore, CAP could correlate with these proxies across the SE if altered, but this is not observed in our

samples^{29,30} (Extended Data Table 1 and Fig. 1). Furthermore, coexisting $\delta^{34}\text{S}$ values in carbonate-associated sulfate (CAS; $\delta^{34}\text{S}_{\text{CAS}}$) decline throughout the SE^{20–22,24} (Fig. 1b–d), which is inconsistent with known diagenetic pore-water chemistry and the increasingly elevated $\delta^{34}\text{S}_{\text{CAS}}$ values that commonly occur in diagenetic carbonates owing to microbial sulfate reduction³³. Furthermore, local redox proxies (for example, I/(Ca+Mg), Ce/Ce*, Fe speciation) measured among globally distributed SE sections record differing local redox conditions^{34–36}, which is also inconsistent with a global diagenetic pathway (see Supplementary Information 3). Finally, $^{87}\text{Sr}/^{86}\text{Sr}$ values and trends in the Cerro Rajón and Death Valley sections reflect local diagenetic alteration (see Supplementary Information 2), yet preserve similar CAP trends to other SE sections (Fig. 1).

Notably, calcite and dolomite minerals in the study sections have undergone different diagenetic pathways and may have differences in distribution coefficients for CAP²⁹. Despite this, CAP trends remain consistent among sections regardless of whether they are hosted in calcite or dolomite minerals (Fig. 1b–g). This strongly argues against a dominant diagenetic and mineralogical control on the CAP trends and therefore we conclude that the CAP trends observed in this study most probably represent primary changes in seawater chemistry, although diagenetic alteration of local CAP values may have exerted a minor influence. However, we note that, as well as diagenetic processes, changes in ocean pH, alkalinity, temperature and carbonate precipitation can all affect CAP values without concomitant changes in oceanic phosphate concentrations. We consider all of these potentially influencing factors on our CAP data in Supplementary Information 3, 4 and 9 and find that changes in oceanic P concentration is the most plausible overarching control on the global CAP trends that we observe, albeit with possible minor overprints from changes in seawater chemistry.

Given the lower-than-mantle $\delta^{13}\text{C}_{\text{carb}}$ values of the SE, some models that report the SE as a primary seawater signal have centred on oxidation of an organic-matter reservoir, such as dissolved organic matter (DOM)^{37,38}, fossil kerogen²³ or methane³⁹, all of which contain ^{13}C -depleted carbon and, with the exception of methane, also contain P. Assuming that oxidant supply exceeds demand, these models are supported by many redox studies that suggest a transient global oceanic oxidation event during the SE, as supported by potential global-scale redox proxies such as $\delta^{238}\text{U}_{\text{carb}}$ (Fig. 1b–d). Other models have invoked a diagenetic origin or air-sea exchange of CO₂ (ref. 32) for the low $\delta^{13}\text{C}_{\text{carb}}$ values of the SE^{31,40}, but it is difficult to predict how these models could reconcile the coevolving trends of our new CAP data with the $\delta^{13}\text{C}_{\text{carb}}$ and redox proxy trends of the SE (see Supplementary Information 3 and 7).

Here we examine several primary seawater signal hypotheses for the SE (see Supplementary Information 7 and Extended Data Fig. 2 for details). As discussed below, we find that a best-fit solution is achieved when rising oceanic sulfate levels (driven by enhanced weathering) stimulates sulfate-limited microbial sulfate reduction and oxidation of a DOM reservoir³⁷ (Fig. 2). This mechanism is supported by higher values of CAS concentration and lower values of $\delta^{34}\text{S}_{\text{CAS}}$ during the SE^{20–24} (Fig. 1b–d), which are indicative of a growing oceanic sulfate reservoir³⁷. Enhanced weathering (and, accordingly, sulfate supply) during the SE is supported by elevated $^{87}\text{Sr}/^{86}\text{Sr}$ (ref. 41) (Fig. 1b–e) and $\varepsilon\text{Nd}(t)$ records⁴². We quantitatively explore this scenario and its impact on ocean P using the COPSE biogeochemical model (Fig. 3 and Extended Data Figs. 2–7).

It is well documented that the Ediacaran oceans were dominated by deeper anoxic waters^{43,44} and, therefore, free oxygen would have been in contact with a small fraction of the deep-ocean DOM pool. Consequently, sulfate is the primary oxidant in our model. Indeed, if a DOM reservoir was oxidized by free O₂, our modelling indicates that ocean anoxia would not substantially decrease during the SE, which would allow for sustained high ocean P levels resulting from elevated weathering and DOM oxidation (Extended Data Fig. 3). However, this contrasts with coexisting $\delta^{238}\text{U}_{\text{carb}}$ data showing a substantial decrease

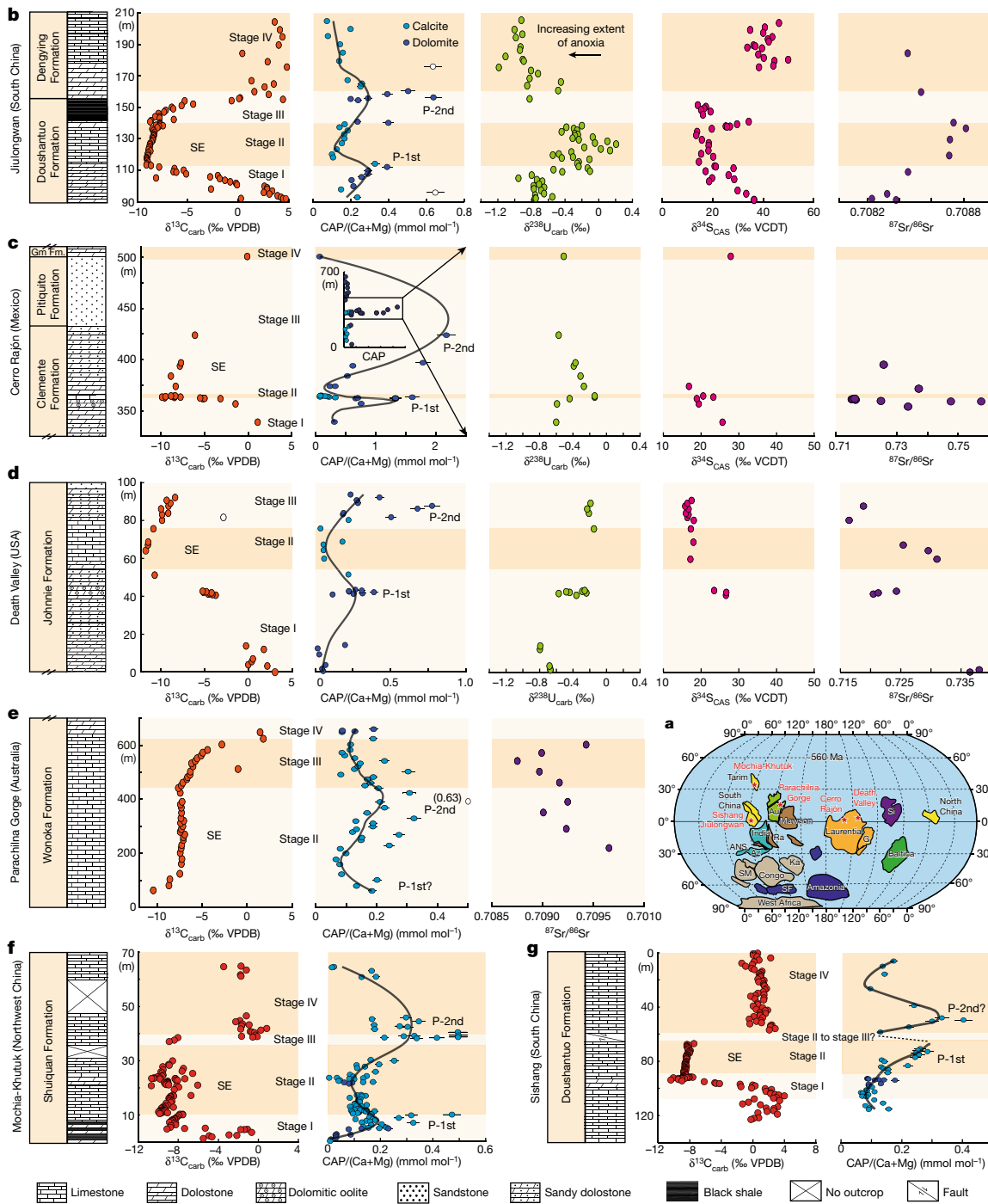


Fig. 1 | CAP (given as CAP/(Ca+Mg)) and accompanying key geochemical records in six globally distributed sections that record the SE, the largest known negative C-isotope excursion in carbonate ($\delta^{13}\text{C}_{\text{carb}}$) from the geological record. **a**, Global palaeogeographic map showing the locations of study regions (red stars) at around 560 Ma, modified after ref. 25. ANS, Arabian–Nubian Shield; Au, Australia; Az, Azania; G, Greenland; Ka, Kalahari; Ra, Rayner (Antarctica); SF, São Francisco; Si, Siberia; SM, Sahara Metacraton. **b**, Jiulongwan section (South China). **c**, Cerro Rajón section (Mexico). Inset graph shows extended section. **d**, Death Valley section (USA). **e**, Parachilna Gorge section (Australia). **f**, Mochia-Khutuk section (Northwest China). **g**, Sishang section (South China). Geochemical data sources: CAP and $^{87}\text{Sr}/^{86}\text{Sr}$ data are from this study; also, $\delta^{13}\text{C}_{\text{carb}}$ of the Sishang and Parachilna Gorge sections are data from this study; other C-isotope, U-isotope and S-isotope data from

refs. 7,8,21–24,26,27. P-1st, first CAP peak; P-2nd, second CAP peak. Gm Fm., Gamuza Formation; VCDT, Vienna Canyon Diablo Troilite. Stratigraphic heights are metres above the first exposed outcrops of Ediacaran strata, except in the Death Valley, Parachilna Gorge and Mochia-Khutuk sections, which are metres above the lower boundary of the measured geological formation and in the Sishang section, which are metres below the Dengying Formation. Light blue circles are $\delta^{13}\text{C}_{\text{carb}}$ and CAP outliers and error bars show a 5% error margin. Black line through CAP data denotes locally weighted scatter plot smoothing. Stages I–IV are defined as follows: stage I (falling limb of $\delta^{13}\text{C}_{\text{carb}}$), stage II (plateau of $\delta^{13}\text{C}_{\text{carb}}$ values), stage III (rising limb of $\delta^{13}\text{C}_{\text{carb}}$) and stage IV (return to pre-SE $\delta^{13}\text{C}_{\text{carb}}$ values). See Supplementary Information 2 for correlation between sections and published data.

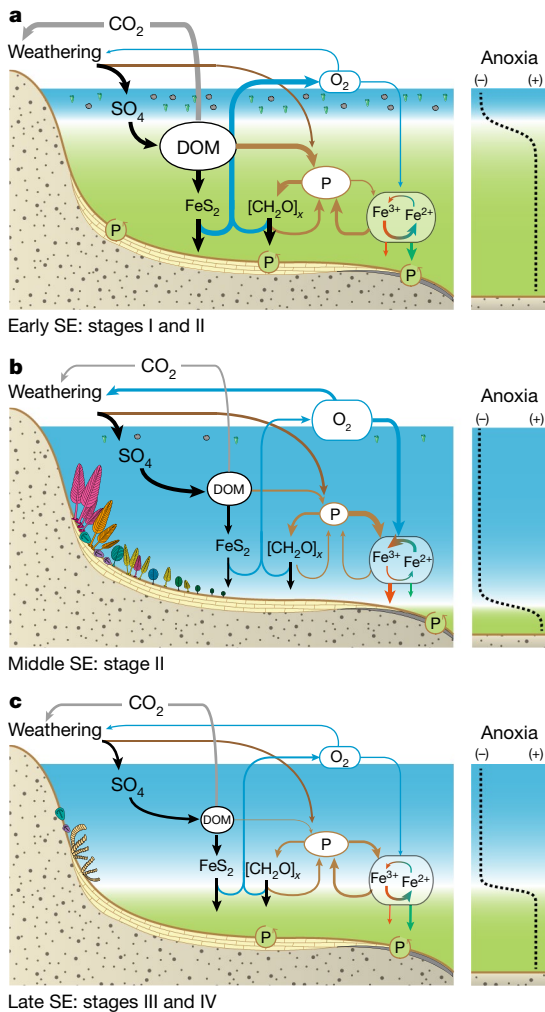


Fig. 2 | Conceptual model illustrating the coevolution of the phosphorus cycle and DOM oxidation during the SE (see text for detailed description of the panels). **a**, Increasing oceanic sulfate from weathering oxidizes oceanic DOM, increasing oceanic P and atmospheric O_2 and CO_2 . **b**, Elevated atmospheric O_2 decreases ocean anoxia and increases sedimentary P burial. **c**, Cessation of DOM oxidation and organic-pyrite burial leads to a decrease in atmospheric O_2 and the return of ocean anoxia. Stages I–IV refer to SE stages I–IV in Fig. 1. Arrows from Fe^{2+} and Fe^{3+} signify the burial of P with Fe under anoxic and oxic conditions.

in ocean anoxia, as well as the CAP records showing a drop in oceanic P levels during the SE^{8,35} (Fig. 1b–g). Similarly, models for DOM oxidation by a combination of sulfate and free O_2 are also inconsistent with the observed $\delta^{238}\text{U}_{\text{carb}}$ -CAP records (Extended Data Fig. 3).

The sizes of the modelled DOM reservoir and sulfate pulse to the oceans were adjusted to produce a SE with a duration of 15 million years (Myr) (see Supplementary Information 5), while also reproducing the two observed CAP peaks (Extended Data Figs. 4–6; P-1st and P-2nd in Fig. 1). Varying the magnitude of the extra sulfate pulse to the oceans has little effect on modelled CAP trends, whereas burying all the extra sulfate as pyrite creates a $p\text{O}_2$ trend inconsistent with redox proxies from the SE (Extended Data Fig. 5). Similarly, if gypsum is assumed not to covary with seawater sulfate levels, increasing sulfate levels prevent a return to anoxia after the SE, which is inconsistent with coexisting $\delta^{238}\text{U}_{\text{carb}}$ and $\delta^{34}\text{S}_{\text{CAS}}$ records (Extended Data Fig. 5). Finally, to best fit our CAP data, we suppressed oceanic P levels in the COPSE model under anoxia by assuming that P is also buried in association with Fe^{2+} , rather than only with Fe^{3+} (Fig. 3; also see Extended Data Fig. 7 for model results with no Fe^{2+} -associated P burial). This

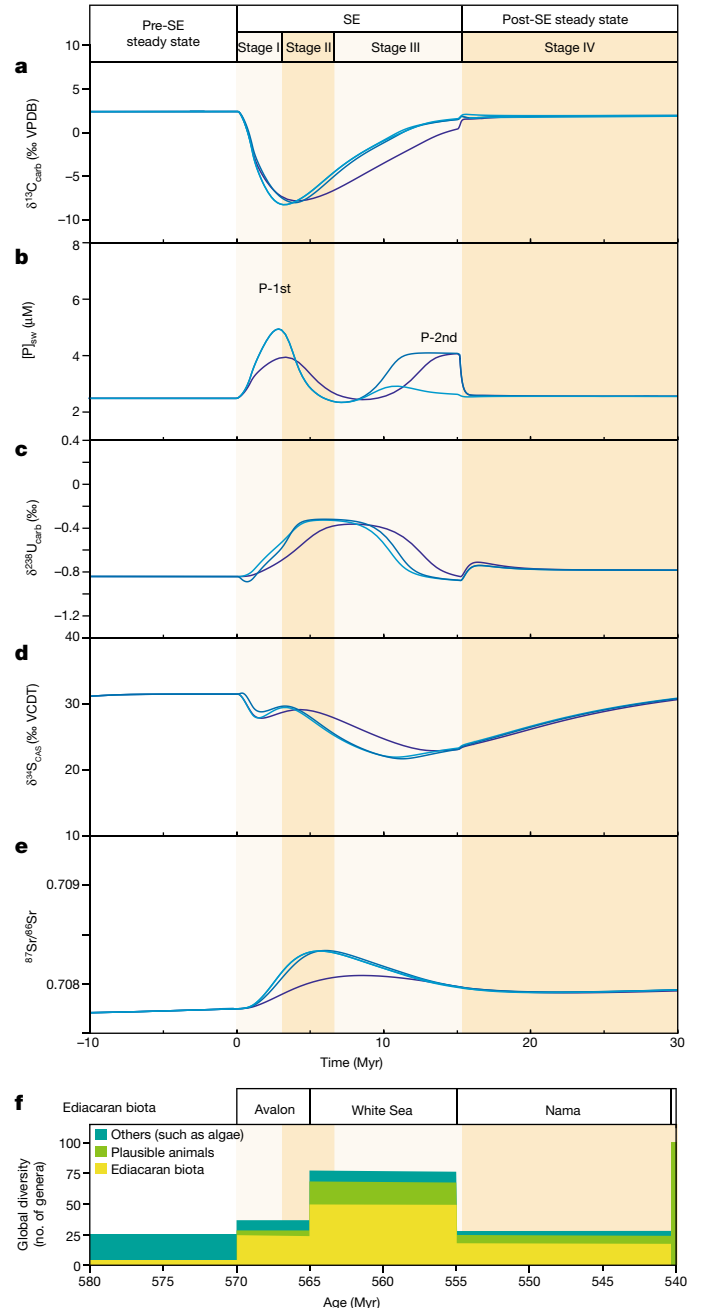


Fig. 3 | Biogeochemical quantitative model results that best replicate the observed CAP and C-, U-, S- and Sr-isotope records in Fig. 1. **a**, Ocean carbonate carbon isotopic composition ($\delta^{13}\text{C}_{\text{carb}}$). **b**, Ocean P concentration ($[P]_{\text{sw}}$). **c**, Ocean carbonate uranium isotopic composition ($\delta^{238}\text{U}_{\text{carb}}$). **d**, Ocean sulfate sulfur isotopic composition ($\delta^{34}\text{S}_{\text{CAS}}$). VCDT, Vienna Canyon Diablo Troilite. **e**, Ocean carbonate strontium isotopic composition ($\delta^{87}\text{Sr}/\delta^{86}\text{Sr}$). **f**, Ediacaran fossil record (adapted after ref. 19). Note the different time axes of panels **a**–**e** from panel **f**. Stages I–IV and P-1st and P-2nd refer to SE $\delta^{13}\text{C}_{\text{carb}}$ profile and CAP peaks in Fig. 1, respectively. Turquoise lines represent model run with continuous Fe^{2+} -P burial and no HCO_3^- release from DOM oxidation; blue lines represent Fe^{2+} -P burial stops during SE and no HCO_3^- release from DOM oxidation; dark blue lines represent Fe^{2+} -P burial stops during SE and HCO_3^- released during DOM oxidation, which halves CO_2 release from DOM (see Supplementary Information 4 and 6 for details).

choice is based on the predominantly ferruginous ocean conditions in the late Neoproterozoic and previous suggestions that ferruginous oceans may have drawn down ocean P through uptake by means of a variety of Fe mineral precipitates^{6,15,17}. The relative magnitudes of the

modelled ocean P peaks were varied by changing the onset and waning of Fe²⁺-P burial and whether HCO₃⁻ is released alongside CO₂ during sulfate reduction of DOM (Fig. 3). Details and rationale for the model choices are provided in Methods and Supplementary Information 6–8.

Our quantitative modelling indicates that the SE CAP profiles may have recorded feedbacks in weathering, organic matter burial/oxidation and the extent of marine anoxia that bridges previously elusive δ¹³C and palaeoredox proxy relationships. We detail the scenario below: (1) further sulfate input to the oceans from weathering triggers the oxidation of a DOM reservoir by sulfate at the beginning of the SE (Fig. 2a). This released organic-bound C and P led to declining oceanic δ¹³C and increased oceanic P as well as atmospheric pCO₂, thereby elevating P input to the oceans through silicate weathering (stage I and P-1st in Figs. 1b–g and 3b). CO₂-driven weathering also resulted in an elevated ⁸⁷Sr/⁸⁶Sr curve across the SE⁴¹ (Figs. 1b–e and 3d). (2) Greater P availability would then elevate primary productivity and concomitant organic matter and pyrite burial, which increased pO₂ (Fig. 2a) and decreased the extent of ocean anoxia (Fig. 2b), as suggested by the observed global shift to more positive δ²³⁸U values (Figs. 1b–d and 3c). (3) A decrease in ocean anoxia would increase P burial and lead to a decrease in the oceanic P reservoir (Fig. 2b), consistent with declining CAP values and coincident maximum δ²³⁸U values (stage II in Figs. 1b–g and 3b,c). (4) As the size of the DOM reservoir dwindled, oceanic δ¹³C would start to return to pre-SE values (stage III in Figs. 1b–g and 3a). Simultaneously, decreasing organic and pyrite burial drove atmospheric oxygen lower, which is supported by a reduced P reservoir and, consequently, lower rates of oxygenic photosynthesis, resulting in lower pO₂ levels and increasing marine anoxia (Fig. 2c), which may be recorded by a transition to increasingly negative δ²³⁸U values^{8,45} (stage III in Figs. 1b–d and 3c). Other independent carbonate-hosted and siliciclastic-hosted redox proxies (for example, Tl and Mo isotopes^{46,47}, carbonate-bound iodate³⁵ and Fe speciation³⁶) corroborate the increase after a previous decrease in ocean anoxia across the SE. Increasing ocean anoxia would decrease P burial, which, when coupled with continued P release from DOM and weathering, would lead to another increase in the P reservoir (Fig. 2c), as observed in the CAP data (P-2nd in Figs. 1b–g and 3b). (5) Finally, cessation of massive DOM oxidation and reduced continental weathering led to a waning P input from DOM and continental weathering, which—in turn—decreased organic and pyrite burial, supporting a return of elevated anoxia, as evidenced by negative δ²³⁸U values during the terminal SE in several global carbonate sections^{7,9} and a return to pre-SE δ¹³C_{carb} values and coexisting low CAP values (stage IV in Figs. 1b–g and 3a–c).

An alternative to DOM oxidation could be methane oxidation²³ by sulfate. However, anaerobic oxidation of methane is less likely because methane oxidation will not release P directly and is unlikely to lead to pCO₂ increases (and, thus, elevated P weathering), favouring alkalinity increases instead. The possibility of small temporal differences in our δ¹³C_{carb} and CAP trends among globally distributed sections (Fig. 1) may have resulted from heterogeneous redox conditions in the Ediacaran, which led to variable spatiotemporal rates of DOM oxidation, continental weathering and element cycling²². Consequently, we conclude that our CAP data, in cohort with coexisting C, S, U and Sr isotopic data, as well as other redox proxies, are best explained by the oxidation of an organic-matter reservoir (DOM or fossil organic matter) by sulfate and resulting organic and pyrite burial, which facilitated ocean oxygenation and perhaps the coeval diversification of complex life in the Ediacaran^{18,19} (Fig. 3e).

The CAP proxy predominantly records local seawater P levels, reflecting P fluxes from surrounding sediments, riverine input, ocean upwelling and so on. Whether local seawater P levels are controlled by local or global processes will depend on the magnitude of fluxes involved at different timescales. Observations of long-term oceanic P cycling suggest that upwelling of deep-ocean P onto continental shelves is quantitatively larger than local continental-shelf P fluxes¹⁰.

This can be demonstrated using a quantitative four-box ocean P cycle model, which predicts that continental-shelf P concentrations, apart from the most proximal areas and mixed layer, track deep ocean P levels over geological timescales, owing to the supply of P from upwelling^{3,13} (Extended Data Fig. 8). Given the relatively homogenous concentration of deep-ocean P and a residence time greater than the oceanic mixing time¹⁰, upwelling of deep-ocean P is expected to result in continental-shelf P concentrations that capture overall P levels in the global ocean when viewed over geological timescales. Consequently, our CAP trends from continental shelves are expected to represent global changes in the average ocean P concentration over geological timescales and their global relationships are thus preserved despite the potential for local overprints that include redox controls on continental-shelf P concentrations (see Supplementary Information 8). This view is supported by similar CAP trends among our global sections, despite having been deposited under differing local redox conditions^{34,35}.

Given that CAP and δ²³⁸U_{carb} trends may reflect relative changes in the average global ocean P concentration and extent of ocean-floor anoxia, respectively, our study provides a unique opportunity to explore dynamics in the Ediacaran P and O₂ cycles. As predicted by observations of modern aquatic environments, expansion of oxygenated bottom waters during the SE (evidenced by δ²³⁸U_{carb}) is accompanied by declines in marine P concentration (as seen in CAP). Surprisingly, however, minimal extents of ocean-floor anoxia (that is, the most positive δ²³⁸U_{carb} values in stage II of the SE) are associated with CAP values of equal magnitude to those CAP values during periods of maximum ocean-floor anoxia before/after the SE (that is, the most negative δ²³⁸U_{carb} values in the early stage I and stage IV) at all studied sections (Fig. 1b–d). This observation is in stark contrast to modern P and O₂ cycling, in which widespread ocean-floor anoxia supports higher ocean P levels relative to periods with limited ocean-floor anoxia. Similarly, δ²³⁸U_{carb} and CAP covary, increasing and decreasing at the start and end of the SE, respectively (Fig. 1b–e), which also contrasts with canonical models of modern P and O₂ cycles. This difference indicates that the Ediacaran P and O₂ cycles may have fundamentally differed to modern cycles^{1–3,11} (Fig. 3b,c and Extended Data Fig. 7). Note that this conclusion is based on the comparison of CAP values from discrete intervals when δ²³⁸U_{carb} data are at their maximum and minimum and, therefore, a precise temporal correlation of CAP trends among the studied sections does not affect the conclusions. Moreover, CAP and δ²³⁸U_{carb} were measured in identical sample powders and minerals, ruling out effects of temporal or mineralogical differences.

One may argue that P fluxes from continental weathering and organic-matter oxidation could have maintained high ocean P levels during the SE, effectively balancing the increased P sinks under oxygenated bottom waters. However, current quantitative models of P and O₂ cycling indicate that, even under the most extreme P-input fluxes, oceanic P levels are still expected to be lower during minimal oceanic anoxia during the SE relative to before or after the SE when the extent of seafloor anoxia was greater (see Extended Data Fig. 4 and Supplementary Information 9). Furthermore, modelling and experimental results indicate that changes in ocean pH, alkalinity or carbonate-precipitation rate resulting from shifts in surface weathering, pCO₂ and organic remineralization are unlikely to have decoupled the CAP and δ²³⁸U_{carb} values (see Extended Data Fig. 9 and Supplementary Information 4 and 9).

The roughly equivalent oceanic P levels under maximum and minimum extents of ocean-floor anoxia across the SE provides the first direct observation for a decoupling of the modern-style negative-feedback cycles between oceanic P and O₂. At present, there are no other coupled datasets of CAP and δ²³⁸U_{carb} that capture a modern-style P and O₂ cycle to which we can compare our dataset. However, chemical traits of redox-dependant phosphorus burial are frequently observed in Phanerozoic sediments^{2,11,12} but largely absent in Ediacaran sediments deposited under ferruginous conditions⁴⁸, which may support our

conclusion of decoupled P and O₂ cycles in Ediacaran oceans. For example, C_{org}/P_{Tot} (total sediment organic carbon/total sediment P) values are roughly invariant among siliciclastic sediments deposited under variable redox conditions in the Ediacaran Doushantuo Formation⁴⁸, whereas C_{org}/P_{Tot} commonly covaries with local redox conditions in Phanerozoic sediments^{2,11,12}.

Although we favour a primary seawater signal as described above, and cannot entirely rule out an early diagenetic interpretation of the CAP trends, such a scenario is unlikely to change our conclusion of decoupled P and O₂ cycling in the Ediacaran ocean. This is because, in modern marine sediments, increasingly ¹³C-depleted pore waters carry increasingly higher P concentrations following the remineralization of organic matter. Therefore, if carbonate deposited during the SE indeed captured diagenetic pore-water chemistry, the more ¹³C-depleted fluids (down to -12‰) should have carried higher solution P concentrations relative to fluids surrounding carbonate deposited before or after the SE with high δ¹³C_{carb} values (up to +5‰). However, carbonates with these endmember δ¹³C_{carb} values across the SE carry equable CAP values (Fig. 1b–g). According to our early diagenetic model (Supplementary Information 3), to achieve a δ¹³C_{carb} shift from +5 to -12‰ in diagenetic carbonates, CAP is expected to increase by at least a factor of four, yet plots of our δ¹³C_{carb} and CAP data show no such trend (Extended Data Fig. 1d). This decoupling between δ¹³C_{carb} and CAP required substantial sequestration of P released from diagenetic organic remineralization in reducing Ediacaran pore waters (directly evidenced by bottom-water redox proxies, for example, Fe speciation data across the interval of highly depleted δ¹³C values in the Jiulongwan section⁴³). This P sequestration in anoxic pore waters (and Ediacaran water columns)^{43,44} is also in stark contrast to modern P and O₂ cycling, thus supporting a decoupled P and O₂ cycle in the Ediacaran (see more detailed discussion in Supplementary Information 3). Moreover, purported models for the SE that achieve low δ¹³C in seawater by means of non-DOM-oxidation mechanisms³² still advocate for carbonate deposited during the SE to have captured seawater chemistry. Consequently, the observed CAP and δ²³⁸U_{carb} trends would be faithful recorders of seawater chemistry and, therefore, support the conclusion of decoupled P and O₂ cycles in the Ediacaran.

The decoupling of ocean P recycling and anoxia observed here probably results from persistent P removal by organic or iron-mineral phases under widespread oxidant-depleted, ferruginous conditions in Ediacaran oceans¹⁶. Given similar redox conditions and potentially a small P reservoir in Precambrian oceans preceding the Ediacaran⁴⁹, it is reasonable to infer that such a decoupling of the P and O₂ cycles may have existed throughout most of the Precambrian⁵⁰. Notably, a weakening of the oceanic P and O₂ feedbacks as suggested here would have locked the Precambrian oceans and atmosphere into a largely anoxic state, because ocean anoxia would not have resulted in elevated marine P availability, oxygenic photosynthesis and organic-matter burial relative to periods of lower marine anoxia. Consequently, Precambrian oceanic oxygenation events, such as the SE and possibly others (for example, the Great Oxygenation Event⁵⁰), may have relied on external stimuli such as sulfate weathering inputs rather than internal oceanic P–O₂ cycling alone^{4,5}. This may explain the prolonged rise of oxygen and complex life over Earth history until the removal of widespread ferruginous conditions or increases in sulfate/oxidant availability in the Phanerozoic, which shifted the Ediacaran P and O₂ cycles into a modern-style, negative-feedback cycle¹. In turn, this transition may explain the prolonged oxygenation and metazoan habitation of the Phanerozoic oceans¹.

Online content

Any methods, additional references, Nature Portfolio reporting summaries, source data, extended data, supplementary information, acknowledgements, peer review information; details of author contributions

and competing interests; and statements of data and code availability are available at <https://doi.org/10.1038/s41586-023-06077-6>.

- Van Cappellen, P. & Ingall, E. D. Redox stabilization of the atmosphere and oceans by phosphorus-limited marine productivity. *Science* **271**, 493–496 (1996).
- Algeo, T. J. & Ingall, E. Sedimentary C_{org}:P ratios, paleocean ventilation, and Phanerozoic atmospheric pO₂. *Palaeogeogr. Palaeoclimatol. Palaeoecol.* **256**, 130–155 (2007).
- Slomp, C. P. & Van Cappellen, P. The global marine phosphorus cycle: sensitivity to oceanic circulation. *Biogeochemistry* **4**, 155–171 (2007).
- Laakso, T. A., Sperling, E. A., Johnston, D. T. & Knoll, A. H. Ediacaran reorganization of the marine phosphorus cycle. *Proc. Natl. Acad. Sci.* **117**, 11961 (2020).
- Kipp, M. A. & Stüeken, E. E. Biomass recycling and Earth's early phosphorus cycle. *Sci. Adv.* **3**, eaao4795 (2017).
- Reinhard, C. T. et al. Evolution of the global phosphorus cycle. *Nature* **541**, 386–389 (2017).
- Zhang, F. et al. Extensive marine anoxia during the terminal Ediacaran Period. *Sci. Adv.* **4**, eaan8983 (2018).
- Zhang, F. et al. Global marine redox changes drove the rise and fall of the Ediacara biota. *Geobiology* **17**, 594–610 (2019).
- Tostevin, R. et al. Uranium isotope evidence for an expansion of anoxia in terminal Ediacaran oceans. *Earth Planet. Sci. Lett.* **506**, 104–112 (2019).
- Ruttenberg, K. C. in *Treatise on Geochemistry* Vol. 8 (eds Holland, H. D. & Turekian, K. K.) 585–643 (Pergamon, 2003).
- Ingall, E. D., Bustin, R. M. & Van Cappellen, P. Influence of water column anoxia on the burial and preservation of carbon and phosphorus in marine shales. *Geochim. Cosmochim. Acta* **57**, 303–316 (1993).
- Xiong, Y. et al. Phosphorus cycling in Lake Cadagno, Switzerland: a low sulfate euxinic ocean analogue. *Geochim. Cosmochim. Acta* **251**, 116–135 (2019).
- Alcott, L. J., Mills, B. J. W. & Poultton, S. W. Stepwise Earth oxygenation is an inherent property of global biogeochemical cycling. *Science* **366**, 1333–1337 (2019).
- Planavsky, N. J. et al. The evolution of the marine phosphate reservoir. *Nature* **467**, 1088–1090 (2010).
- Bjerrum, C. J. & Canfield, D. E. Ocean productivity before about 1.9 Gyr ago limited by phosphorus adsorption onto iron oxides. *Nature* **417**, 159–162 (2002).
- Jones, C., Nomosatyro, S., Crowe, S. A., Bjerrum, C. J. & Canfield, D. E. Iron oxides, divalent cations, silica, and the early earth phosphorus crisis. *Geology* **43**, 135–138 (2015).
- Derry, L. A. Causes and consequences of mid-Proterozoic anoxia. *Geophys. Res. Lett.* **42**, 8538–8546 (2015).
- Evans, S. D., Diamond, C. W., Droser, M. L. & Lyons, T. W. Dynamic oxygen and coupled biological and ecological innovation during the second wave of the Ediacara Biota. *Emerg. Top. Life Sci.* **2**, 223–233 (2018).
- Darroch, S. A. F., Smith, E. F., Laflamme, M. & Erwin, D. H. Ediacaran extinction and Cambrian explosion. *Trends Ecol. Evol.* **33**, 653–663 (2018).
- Fike, D. A., Grotzinger, J. P., Pratt, L. M. & Summons, R. E. Oxidation of the Ediacaran ocean. *Nature* **444**, 744–747 (2006).
- Shi, W. et al. Sulfur isotope evidence for transient marine-shelf oxidation during the Ediacaran Shuram Excursion. *Geology* **46**, 267–270 (2018).
- Li, C. et al. Uncovering the spatial heterogeneity of Ediacaran carbon cycling. *Geobiology* **15**, 211–224 (2017).
- Kaufman, A. J., Corsetti, F. A. & Varni, M. A. The effect of rising atmospheric oxygen on carbon and sulfur isotope anomalies in the Neoproterozoic Johnnie Formation, Death Valley, USA. *Chem. Geol.* **237**, 47–63 (2007).
- Loyd, S. J. et al. Sustained low marine sulfate concentrations from the Neoproterozoic to the Cambrian: insights from carbonates of northwestern Mexico and eastern California. *Earth Planet. Sci. Lett.* **339–340**, 79–94 (2012).
- Meredith, A. S. et al. A full-plate global reconstruction of the Neoproterozoic. *Gondwana Res.* **50**, 84–134 (2017).
- Huang, K. et al. Interaction of Shubertan Biota and environment in the terminal Ediacaran ocean: evidence from I/(Ca+Mg) and sulfur isotopes. *Precambrian Res.* **379**, 106814 (2022).
- Wang, R. et al. A great late Ediacaran ice age. *Natl. Sci. Rev.* <https://doi.org/10.1093/nsr/nwad117> (2023).
- Rooney, A. D. et al. Calibrating the coevolution of Ediacaran life and environment. *Proc. Natl. Acad. Sci.* **117**, 16824–16830 (2020).
- Dodd, M. S. et al. Development of carbonate-associated phosphate (CAP) as a proxy for reconstructing ancient ocean phosphate levels. *Geochim. Cosmochim. Acta* **301**, 48–69 (2021).
- Shimura, T. et al. In-situ analyses of phosphorus contents of carbonate minerals: reconstruction of phosphorus contents of seawater from the Ediacaran to early Cambrian. *Gondwana Res.* **25**, 1090–1107 (2014).
- Swart, P. K. & Kennedy, M. J. Does the global stratigraphic reproducibility of δ¹³C in Neoproterozoic carbonates require a marine origin? A Pliocene–Pleistocene comparison. *Geology* **40**, 87–90 (2012).
- Busch, J. F. et al. Global and local drivers of the Ediacaran Shuram carbon isotope excursion. *Earth Planet. Sci. Lett.* **579**, 117368 (2022).
- Loyd, S. J., Berelson, W. M., Lyons, T. W., Hammond, D. E. & Corsetti, F. A. Constraining pathways of microbial mediation for carbonate concretions of the Miocene Monterey Formation using carbonate-associated sulfate. *Geochim. Cosmochim. Acta* **78**, 77–98 (2012).
- Cheng, M. et al. Barite in the Ediacaran Doushantuo Formation and its implications for marine carbon cycling during the largest negative carbon isotope excursion in Earth's history. *Precambrian Res.* **368**, 106485 (2022).
- Hardisty, D. S. et al. Perspectives on Proterozoic surface ocean redox from iodine contents in ancient and recent carbonates. *Earth Planet. Sci. Lett.* **463**, 159–170 (2017).
- Wood, R., Bowyer, F., Penny, A. & Poultton, S. W. Did anoxia terminate Ediacaran benthic communities? Evidence from early diagenesis. *Precambrian Res.* **313**, 134–147 (2018).
- Shields, G. A. et al. Unique Neoproterozoic carbon isotope excursions sustained by coupled evaporite dissolution and pyrite burial. *Nat. Geosci.* **12**, 823–827 (2019).

Article

38. Rothman, D. H., Hayes, J. M. & Summons, R. E. Dynamics of the Neoproterozoic carbon cycle. *Proc. Natl Acad. Sci.* **100**, 8124 (2003).
39. Bjerrum, C. J. & Canfield, D. E. Towards a quantitative understanding of the late Neoproterozoic carbon cycle. *Proc. Natl Acad. Sci.* **108**, 5542 (2011).
40. Derry, L. A. A burial diagenesis origin for the Ediacaran Shuram–Wonoka carbon isotope anomaly. *Earth Planet. Sci. Lett.* **294**, 152–162 (2010).
41. Sawaki, Y. et al. The Ediacaran radiogenic Sr isotope excursion in the Doushantuo Formation in the Three Gorges area, South China. *Precambrian Res.* **176**, 46–64 (2010).
42. Wei, G.-Y. et al. Long-term evolution of terrestrial inputs from the Ediacaran to early Cambrian: clues from Nd isotopes in shallow-marine carbonates, South China. *Palaeogeogr. Palaeoclimatol. Palaeoecol.* **535**, 109367 (2019).
43. Li, C. et al. A stratified redox model for the Ediacaran ocean. *Science* **328**, 80 (2010).
44. Canfield, D. E. et al. Ferruginous conditions dominated later Neoproterozoic deep-water chemistry. *Science* **321**, 949 (2008).
45. Li, Z. et al. Transient and stepwise ocean oxygenation during the late Ediacaran Shuram Excursion: insights from carbonate $\delta^{238}\text{U}$ of northwestern Mexico. *Precambrian Res.* **344**, 105741 (2020).
46. Fan, H. et al. Constraining oceanic oxygenation during the Shuram excursion in South China using thallium isotopes. *Geobiology* **18**, 348–365 (2020).
47. Kendall, B. et al. Uranium and molybdenum isotope evidence for an episode of widespread ocean oxygenation during the late Ediacaran Period. *Geochim. Cosmochim. Acta* **156**, 173–193 (2015).
48. Jin, C. et al. Highly heterogeneous “poikiloredox” conditions in the early Ediacaran Yangtze Sea. *Precambrian Res.* **311**, 157–166 (2018).
49. Lyons, T. W., Reinhard, C. T. & Planavsky, N. J. The rise of oxygen in Earth’s early ocean and atmosphere. *Nature* **506**, 307–315 (2014).
50. Alcott, L. J., Mills, B. J. W., Bekker, A. & Poulton, S. W. Earth’s Great Oxidation Event facilitated by the rise of sedimentary phosphorus recycling. *Nat. Geosci.* **15**, 210–215 (2022).

Publisher's note Springer Nature remains neutral with regard to jurisdictional claims in published maps and institutional affiliations.

Springer Nature or its licensor (e.g. a society or other partner) holds exclusive rights to this article under a publishing agreement with the author(s) or other rightsholder(s); author self-archiving of the accepted manuscript version of this article is solely governed by the terms of such publishing agreement and applicable law.

© The Author(s), under exclusive licence to Springer Nature Limited 2023

Methods

Bulk-rock phosphorus analysis

Although altered material could not be completely avoided, fresh pieces of only fine-grained carbonate rock were selected and crushed to a powder. Phosphorus measurements were conducted by dissolving about 50 mg of sample powder using a standard HNO_3 -HF digestion protocol, in which HNO_3 -HF (1:1) and HNO_3 were sequentially added to a 15-ml Teflon bomb at 190 °C until complete digestion was achieved. Distilled HNO_3 and trace-metal-grade HF reagents were used for all samples. The leachates were then measured by inductively coupled plasma mass spectrometry (ICP-MS) using an Agilent 7700x inductively coupled plasma mass spectrometer. Analytical errors were better than $\pm 7\%$ for phosphorus based on duplicate analyses of two USGS standards (BCR-2 and BHVO-2) and two Chinese national standards (GSR1 and GSR5).

Carbon analysis

Total carbon (TC) and TOC were measured using a CS-900 carbon analyser. TC was measured directly by weighing out about 0.1 g of rock powder with iron shavings and tungsten pellets to aid combustion in the analyser. A calcium carbonate carbon standard (AR1034) was analysed after every ten samples to check reproducibility (± 0.1 wt% C; $n = 30$). To measure TOC, an aliquot of sample powder (about 1 g) was reacted with 6 M HCl to decarbonate the sample, rinsed with deionized water to neutral pH, then centrifuged and dried, and finally measured in the analyser as for TC. Total inorganic carbon (TIC) was then calculated by the difference between TC and TOC.

Carbonate carbon- and oxygen-isotope analysis

About 60–300 µg of sample powder was loaded into a vial after drying at 70 °C for 24 h in an argon atmosphere. The samples were then reacted with 100% phosphoric acid under a vacuum at 70 °C for 220 s using a Kiel IV device. The resulting CO_2 was subsequently introduced into a MAT 253 isotope ratio mass spectrometer for isotopic measurements. Delta values were calibrated relative to international reference standard NBS-19 ($\delta^{13}\text{C} = +1.95\text{\textperthousand}$; $\delta^{18}\text{O} = -2.20\text{\textperthousand}$) and Chinese national standard GBW04416 ($\delta^{13}\text{C} = +1.61 \pm 0.03\text{\textperthousand}$; $\delta^{18}\text{O} = 1.59 \pm 0.11\text{\textperthousand}$). Carbon-isotope and oxygen-isotope data for carbonates are reported relative to Vienna Pee Dee Belemnite (VPDB) with a precision better than $\pm 0.1\text{\textperthousand}$ based on duplicate analyses of GBW04416 and the study samples.

Carbonate-associated phosphate analysis

CAP was measured following previously established protocols²⁹. Only samples comprising >50% carbonate were chosen for analysis. On the basis of sample TIC and carbonate mineralogy, sufficient sample powder was weighed out to yield roughly 1 mmol of carbonate. An appropriate amount of 2% vol/vol acetic acid was then added to the powder to dissolve up to 70% of the carbonate. After 30 min, the sample was centrifuged and the leachate was extracted. An aliquot of leachate was taken for major and trace element analyses and measured using an EXPEC 6000 inductively coupled plasma optical emission spectrometer for Ca and Mg and an Agilent 7700x inductively coupled plasma mass spectrometer for trace elements. Analytical errors were better than $\pm 2\%$ for all studied elements based on duplicate analyses of two USGS standards (BCR-2 and BHVO-2) and two Chinese national standards (GSR1 and GSR5). Another aliquot was taken and mixed with H_2SO_4 to achieve a 1 M H_2SO_4 concentration and left for 1 h to remove Ca as CaSO_4 . Then, P was measured by spectrophotometry using the molybdenum blue method at a wavelength of 880 nm, with a relative standard deviation of better than $\pm 5\%$. The sample residue was then washed with 50 ml of 10% NaCl solution buffered to pH 8 with NaHCO_3 for 24 h and P was measured by the molybdenum blue method. This sequence was repeated until P in the wash was below

detection limit (0.05 ppm). The P in the leach and washes were then summed to give CAP, which was then normalized to the Ca and Mg concentrations in the leach. Three Ediacaran dolomite sediments of varying TIC and TOC were run alongside unknown samples to check reproducibility for quality assurance. Repeat CAP measurements were within $\pm 5\%$.

Strontium-isotope analysis

The extraction method for strontium-isotope analysis was based on previous works^{51–53}. Around 0.1 g of sample was weighed out and then washed for 24 h in 10 ml of 1 M ammonium acetate buffered to pH 8 to remove exchangeable strontium. The sample was then centrifuged, the wash discarded and the sample rinsed with Milli-Q water. Subsequently, the sample was partially leached in 2% acetic acid to dissolve 30% of the sample carbonate and left to react overnight. The sample was then centrifuged, the acetic leach discarded and the sample rinsed with Milli-Q water. Following this, a further aliquot of 2% acetic acid was added to dissolve 40% of the sample carbonate and left to react for 30 min. The sample was then centrifuged and the leachate collected for Sr-isotope analysis.

The leachate collected was then centrifuged to remove insoluble residues and then decanted, dried and subsequently dissolved in HNO_3 . Strontium separation by cation exchange was carried out using an automatic column chromatography separation device (see Zhou et al.⁵³ for details). Approximately 200–300 ng of the dried sample was transferred onto a degassed and pre-baked high-purity Re filament with Ta_2O_5 activator. The prepared filaments were measured using the VG Sector 54 thermal ionization mass spectrometer in the Thermal Ionisation Mass Spectrometry facility of China University of Geosciences in Wuhan. Filaments were transferred to a sample carousel, heated under vacuum to a temperature between 1,450 and 1,650 °C and analysed when a stable signal was detected on the mass 88 ion beam. Approximately 100 $^{87}\text{Sr}/^{86}\text{Sr}$ ratio data points were collected for each sample. Final data have been corrected for fractionation using the standard value $^{86}\text{Sr}/^{88}\text{Sr} = 0.1194$. The fraction of ^{87}Sr resulting from in situ decay from ^{87}Rb was removed by measurement of rubidium abundance at mass 85. Repeated analysis of the BCR-2 and BHVO-2 standards yields average values of $^{87}\text{Sr}/^{86}\text{Sr} = 0.70498$ and 0.70347 ± 0.00001 (2σ), respectively, during the analytical window.

Carbonate-precipitation experiments

The precipitation of carbonate and uptake of CAP from seawater solutions followed previous methodologies²⁹. In brief, a peristaltic pump was used to add solutions of 1 M CaCl_2 and 1 M Na_2CO_3 with KH_2PO_4 to 1-litre solutions of synthetic seawater made to emulate modern-day seawater chemistry. Solutions were constantly stirred and an air pump was used to bubble air through the solution to maintain a stable pH. For precipitation-rate experiments, variable amounts of carbonate seeds were used to vary the precipitation rate in conjunction with varying the pump rates of CaCl_2 and Na_2CO_3 . Solution chemistry was checked periodically for pH, alkalinity, calcium and phosphorus concentrations. A Thermo Fisher Scientific pH electrode was used to check the pH with an accuracy better than ± 0.1 units, alkalinity was measured by titration of seawater aliquots with 0.1 M HCl and phosphorus and calcium were measured as outlined above in the ‘CAP analysis’ section. At the end of the experimental run, carbonate was collected by filtration through 0.2-µm PES filters and the carbonate washed with 1 M NaHCO_3 until phosphorus concentrations in the washes were below detection. Once the carbonate samples were clean of adsorbed phosphorus, 0.1 g was completely dissolved in 2 M HCl and the solutions were subsequently analysed for P, Ca and Mg, as outlined above in the ‘CAP analysis’ section. Carbonate-precipitation rates were calculated as $\text{mol m}^{-2} \text{s}^{-1}$ following Barkan et al.⁵⁴.

Article

COPSE biogeochemical modelling

The COPSE model was used to calculate biogeochemical feedbacks between P cycle and DOM oxidation during the SE. This model follows the work of ref. 55 and is solved in MATLAB using the Ordinary Differential Equation (ODE) suite. Here we provide a key description of our model work and the full description of our model work is given in the Supplementary Information.

Steady-state calculation for low background phosphorus concentration under high ocean anoxia in Ediacaran oceans. On the basis of the observed CAP and redox proxy trends across the SE, we can infer that a mechanism(s) was maintaining P at lower levels during the early stage I and stage IV of the SE under high ocean anoxia. Although it is ambiguous what mechanism(s) could maintain a lower P reservoir under anoxia during the Ediacaran^{4–6,15}, we chose to modify iron-bound P burial in the COPSE model (equation (1)) to maintain a low oceanic P reservoir during high ocean anoxia. This is because Fe²⁺-P burial is recognized as a possible P sink in Precambrian ferruginous-dominated oceans (see Supplementary Information 6 for rationale)^{11,14–16}; also, this modification still allows for an increase in oceanic P burial with decreasing ocean anoxia as seen in modern P cycling. We stress that this modification of the COPSE model is a qualitative change, as there are no current quantitative relationships for Fe²⁺-P burial. Notably, this modification does not substantially change the model results between model runs with and without Fe²⁺-P burial, except for lowering ocean P levels under high ocean anoxia (Extended Data Fig. 7). Therefore, this modification is appropriate for this study; however, future modelling work will require field relationships linking enhanced P burial under anoxia to produce more meaningful results. Thus, we modified the flux of iron-bound P burial in the standard COPSE model and include a ferrous iron scavenging flux that has a positive relationship with the degree of anoxia (ANOX) as below:

$$fepb_{sws} = \frac{k_1}{k_2} \cdot \frac{P_t}{P_0} \quad (1)$$

$$fepb_{fe3} = fepb_{sws} \cdot (1 - ANOX) = \frac{k_1}{k_2} \cdot \frac{P_t}{P_0} \cdot (1 - ANOX) \quad (2)$$

$$fepb_{fe2} = (fepb_{sws} - fepb_{fe3}) \cdot ANOX = \frac{k_1}{k_2} \cdot \frac{P_t}{P_0} \cdot ANOX^2 \quad (3)$$

$$fepb_{tot} = fepb_{fe3} + fepb_{fe2} = \frac{k_1}{k_2} \cdot \frac{P_t}{P_0} \cdot (ANOX^2 - ANOX + 1) \quad (4)$$

Here $fepb_{sws}$ is the flux of iron-bound P burial reaching the seawater-sediment interface and $fepb_{fe3}$ is the final flux of P that is buried with Fe³⁺, whereas $fepb_{fe2}$ is the Fe²⁺ scavenging flux including vivianite burial, and $fepb_{tot}$ is the total flux of iron-bound P burial. P_t and P_0 are the masses of the marine P reservoir at time t and present day, respectively. $k_1 = 10^9 \text{ mol P year}^{-1}$ and $k_2 = 0.997527$ are constants, and $0 < ANOX < 0.997527$. This modification changes the original definition of the total iron-bound P burial, which is negatively correlated with anoxia in the standard COPSE model. In practice, this allows for a low ocean P concentration in anoxic-ferruginous Precambrian oceans given a $pO_2 = 0.01 \text{ PAL}$ (see Supplementary Information for details of Fe scavenging). We chose this modelling approach because the simplistic separation of Fe-P burial into Fe²⁺-P and Fe³⁺-P burial allowed us to increase P burial under high ANOX (per the CAP and redox data) while also keeping the original COPSE model P and O₂ cycles in effect.

Weathering sulfate input. We run the COPSE model to steady state, forcing the model conditions to represent the expected geochemical

conditions for the Ediacaran Period. We included a DOM reservoir that responds to a weathering sulfate pulse (sulfate_{pulse}), which uses a simple step-forcing that follows previous work³⁷. The time-dependent forcing function for the sulfate pulse is:

$$\text{sulfate}_{pulse} = \text{interp1}([-10 \ 0 \ 1 \ 15 \ 16 \ 30], [0 \ 0 \ x \ 0 \ 0])$$

in which the first vector is time (Myr) and the second vector is the extra sulfate input relative to the background weathering flux ($x = 3, 4$ or 5). The sulfate pulse is set to last for approximately 15 Myr, which follows the geological ⁸⁷Sr/⁸⁶Sr and εNd(t) records for elevated weathering input during the SE⁴³, as well as following other geological time constraints for the duration of the SE (see Supplementary Information 5 for details on the age framework of the SE). For the model runs in this study, both normal steady-state ‘background’ flux (subscript ‘background’) and extra weathering pulse input (subscript ‘pulse’) are working together and respond to changing geochemical conditions:

$$gypw_{background} = k_{gypw} \cdot U \cdot R \cdot \frac{\text{carbw}}{k_{carbw}} \quad (5)$$

$$gypw_{pulse} = gypw_{background} \cdot \text{sulfate}_{pulse} \quad (6)$$

$$pyrw_{background} = k_{pyrw} \cdot U \cdot R \cdot \frac{\text{carbw}}{k_{carbw}} \quad (7)$$

$$pyrw_{pulse} = pyrw_{background} \cdot \text{sulfate}_{pulse} \quad (8)$$

Here the k_{gypw} and k_{pyrw} are the present-day weathering rates of gypsum and pyrite, respectively, U and R are the normalized uplift and river runoff forcing, respectively and $\frac{\text{carbw}}{k_{carbw}}$ is a climate dependence representing the effect of pCO₂ on global carbonate weathering. For this study, the test case of $x = 5$ is used for our idealized (‘best-fit’) scenario (Extended Data Fig. 6), which maintains a negative δ¹³C_{carb} excursion of around −10‰ for millions of years.

DOM oxidation. The size of the DOM reservoir (model term DOC) is set at the beginning of the model run. This reservoir has an output flux by means of DOM oxidation, which is driven by sulfate reduction³⁷:

$$\frac{d\text{DOC}}{dt} = \begin{cases} 0, & \text{DOC} < 10^{12} \text{ mol} \\ 2 \cdot (gypw_{pulse} + pyrw_{pulse}) \cdot \frac{S_t}{S_0} \cdot \frac{\text{DOC}_t}{\text{DOC}_0}, & \text{DOC} \geq 10^{12} \text{ mol} \end{cases} \quad (9)$$

Here S_t and S_0 are the masses of the marine sulfate reservoirs at time t and present day, respectively, and DOC_t and DOC_0 are the masses of the DOM reservoir at time t and pre-SE, respectively. $\text{DOC}_0 = 30$ times the mass of the modern dissolved inorganic carbon (DIC) reservoir following previous estimation, to maintain a δ¹³C_{carb} excursion of about 15 Myr and reaching values of −10‰. We consider sulfate as the only direct oxidant for DOM oxidation, and its extra pulses set the rate of DOM consumption. The normal background sulfate fluxes are set not to be involved in DOM oxidation but instead balance the oxidation of fresh organic carbon. In nature, free oxygen can also oxidize DOM once its local concentration crosses over a certain threshold (for example, about 4 μM (ref. 56)). We also test this possibility of DOM oxidation by free oxygen using two output fluxes through both sulfate and oxygen, which is given in Extended Data Fig. 3 and Supplementary Information 7. We follow previous models that set DOM oxidation to terminate when the DOM reservoir becomes smaller than 10¹² moles, rather than zero, to prevent system instability³⁷.

Sulfate burial. The COPSE model assumes that marine sulfate is removed by means of the burial of gypsum and pyrite, which are

linearly proportional to the total oceanic sulfate concentration⁵⁵. To balance the extra sulfate input, we add further fluxes of both gypsum (mgsb_{additional}) and pyrite (mpsbt_{additional}) burial, among which the pyrite burial is equal to half the DOM oxidation rate. The remaining sulfate pulse that is not consumed by DOM is assumed to be buried as gypsum:

$$\text{mgsb}_{\text{additional}} = \left(\text{gypw}_{\text{pulse}} + \text{pyrw}_{\text{pulse}} - \frac{\text{dDOC}}{2 \cdot \text{dt}} \right) \cdot \frac{S_t}{S_0} \quad (10)$$

$$\text{mpsbt}_{\text{additional}} = \frac{\text{dDOC}}{2 \cdot \text{dt}} \quad (11)$$

Phosphorus mass balance. In this study, elevated sulfate supply to the Ediacaran ocean, following previous proposals²⁴, is proposed to create a large long-term oxidant source. This input of oxidizing power oxidized a large marine DOM pool, releasing DIC and P. The P released by DOM oxidation (pdoc) is assumed to be a net source for the marine P reservoir, which is calculated using the rate of DOM oxidation ($\frac{\text{dDOC}}{\text{dt}}$) and the C/P_{DOC} ratio. The new P mass is estimated with the following equation, adapted from ref. 55:

$$\frac{dP}{dt} = \text{psea} + \text{pdoc} - \text{mopb} - \text{capb} - \text{fepb}_{\text{tot}} \quad (12)$$

Here psea is the weathering flux of reactive P to the ocean and mopb and capb are P burial with organic carbon and calcium, respectively. We chose a fixed ratio of C/P_{DOC} = 1,000 as the default, but also tested the influence of changing C/P_{DOC} (250, 1,000, 3,500 and no P release) on the marine P concentration (see Extended Data Fig. 4).

Full model description. See Supplementary Information for the full modified COPSE model equations and parameters.

Materials availability

All samples were collected and exported in a responsible manner and in accordance with relevant permits and local laws. Global coordinates and/or location information and drill core names are given for all samples collected in the Supplementary Information files. Requests for materials should be addressed to C.L.

Reporting summary

Further information on research design is available in the Nature Portfolio Reporting Summary linked to this article.

Data availability

All data generated or analysed during this study are available at https://figshare.com/articles/dataset/Dodd_et_al_2023_xlsx/22274293 and included with the published article (and its Supplementary Information files). Source data are provided with this paper.

Code availability

MATLAB code for COPSE is freely available at <https://github.com/bjwmills/COPSE>.

51. Cui, H. et al. Redox architecture of an Ediacaran ocean margin: integrated chemostratigraphic ($\delta^{13}\text{C}$ - $\delta^{34}\text{S}$ - $\delta^{87}\text{Sr}$ -Ce/Ce*) correlation of the Doushantuo Formation, South China. *Chem. Geol.* **405**, 48–62 (2015).
52. Bellefroid, E. J., Planavsky, N. J., Miller, N. R., Brand, U. & Wang, C. Case studies on the utility of sequential carbonate leaching for radiogenic strontium isotope analysis. *Chem. Geol.* **497**, 88–99 (2018).
53. Zhou, F.-Y. et al. Development of an automatic column chromatography separation device for metal isotope analysis based on droplet counting. *Anal. Chem.* **93**, 7196–7203 (2021).
54. Barkan, Y., Paris, G., Webb, S. M., Adkins, J. F. & Halevy, I. Sulfur isotope fractionation between aqueous and carbonate-associated sulfate in abiotic calcite and aragonite. *Geochim. Cosmochim. Acta* **280**, 317–339 (2020).
55. Lenton, T. M., Daines, S. J. & Mills, B. J. W. COPSE reloaded: an improved model of biogeochemical cycling over Phanerozoic time. *Earth Sci. Rev.* **178**, 1–28 (2018).
56. Brüchert, V. et al. Regulation of bacterial sulfate reduction and hydrogen sulfide fluxes in the central Namibian coastal upwelling zone. *Geochim. Cosmochim. Acta* **67**, 4505–4518 (2003).

Acknowledgements We thank B. Shen and R. Wang for generously providing samples from the Mochia-Khutuk section and L. Zheng for assistance in obtaining the Sishang section samples. This study was supported by the NSFC (grant nos. 41825019, 42130208 and 41821001) and the National Key Research and Development Program of China (2022YFF0800100) for funding. M.S.D. acknowledges support from the International Exchange Program for Postdoctors of China and funding from the China Postdoctoral Science Foundation, the Forrest Research Foundation and the University of Western Australia School of Earth Sciences. A.v.S.H. and M.W. acknowledge support from the ARC (DE190100988 and DP210103715). Further funding through the NASA Astrobiology Institute under Cooperative Agreement No. NNA15BB03A issued through the Science Mission Directorate and the Interdisciplinary Consortia for Astrobiology Research (T.W.L.).

Author contributions C.L. led the research. C.L. and M.S.D. designed the research. M.S.D., Z.Z., M.C. and H.G. performed analyses. W.S. and B.J.W.M. conducted modelling work. C.L., T.W.L., D.S.H., S.J.L., M.W.W., A.v.S.H., K.L., M.C. and H.G. provided samples and assistance in the field. S.W.P. provided analytical assistance. M.S.D., C.L. and W.S. wrote the manuscript, with important discussion and contributions from all authors.

Competing interests The authors declare no competing interests.

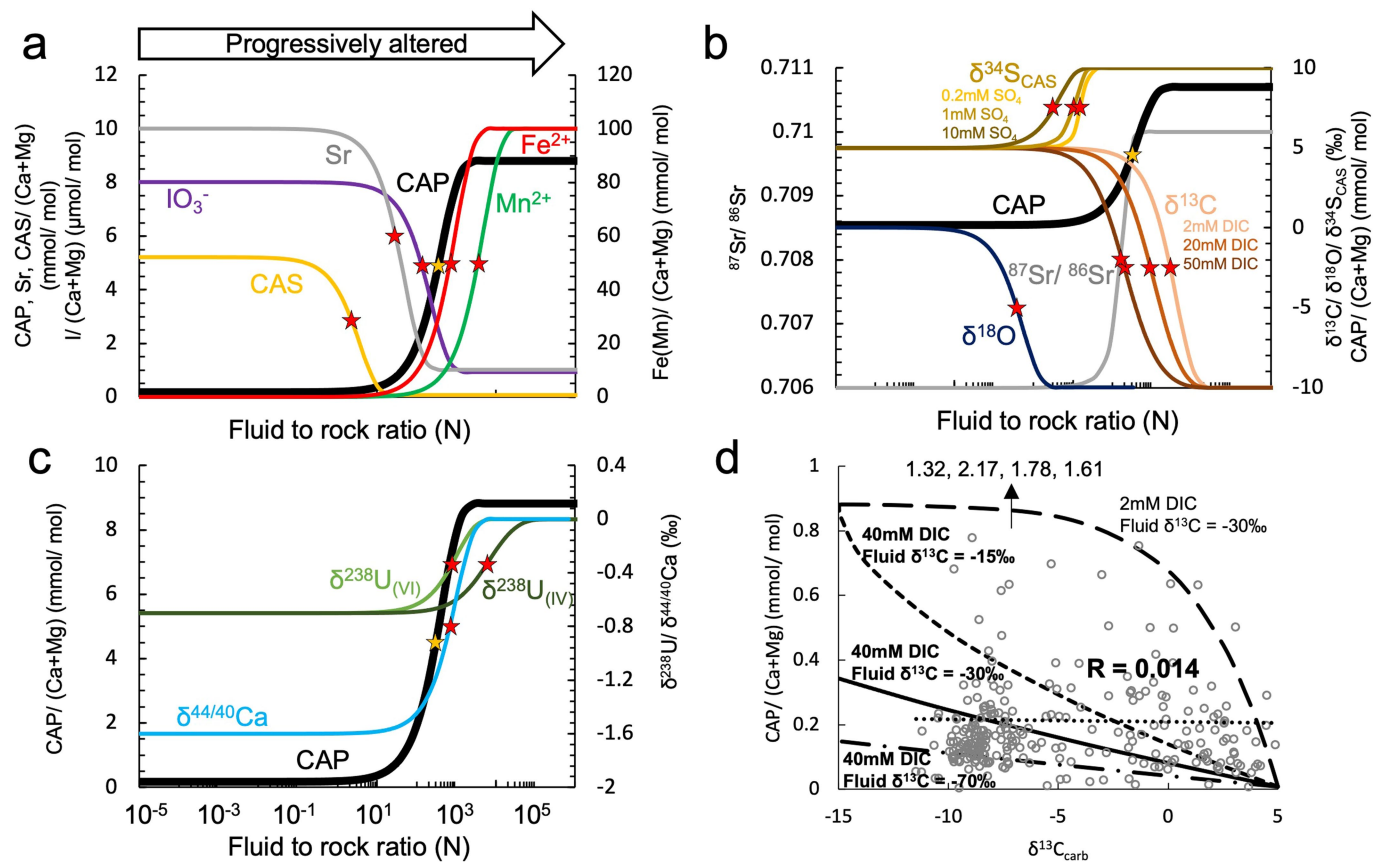
Additional information

Supplementary information The online version contains supplementary material available at <https://doi.org/10.1038/s41586-023-06077-6>.

Correspondence and requests for materials should be addressed to Chao Li.

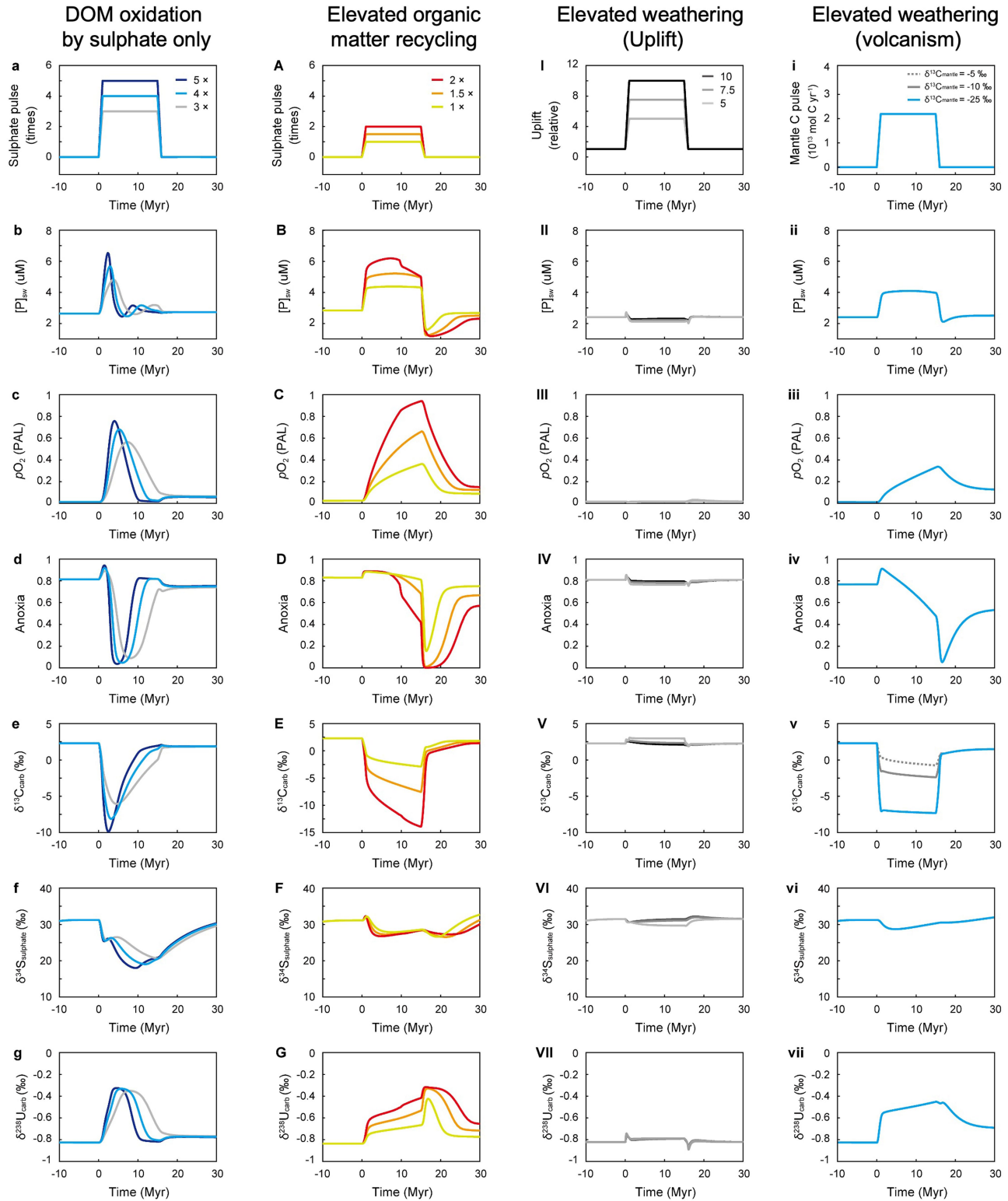
Peer review information *Nature* thanks the anonymous reviewers for their contribution to the peer review of this work.

Reprints and permissions information is available at <http://www.nature.com/reprints>.



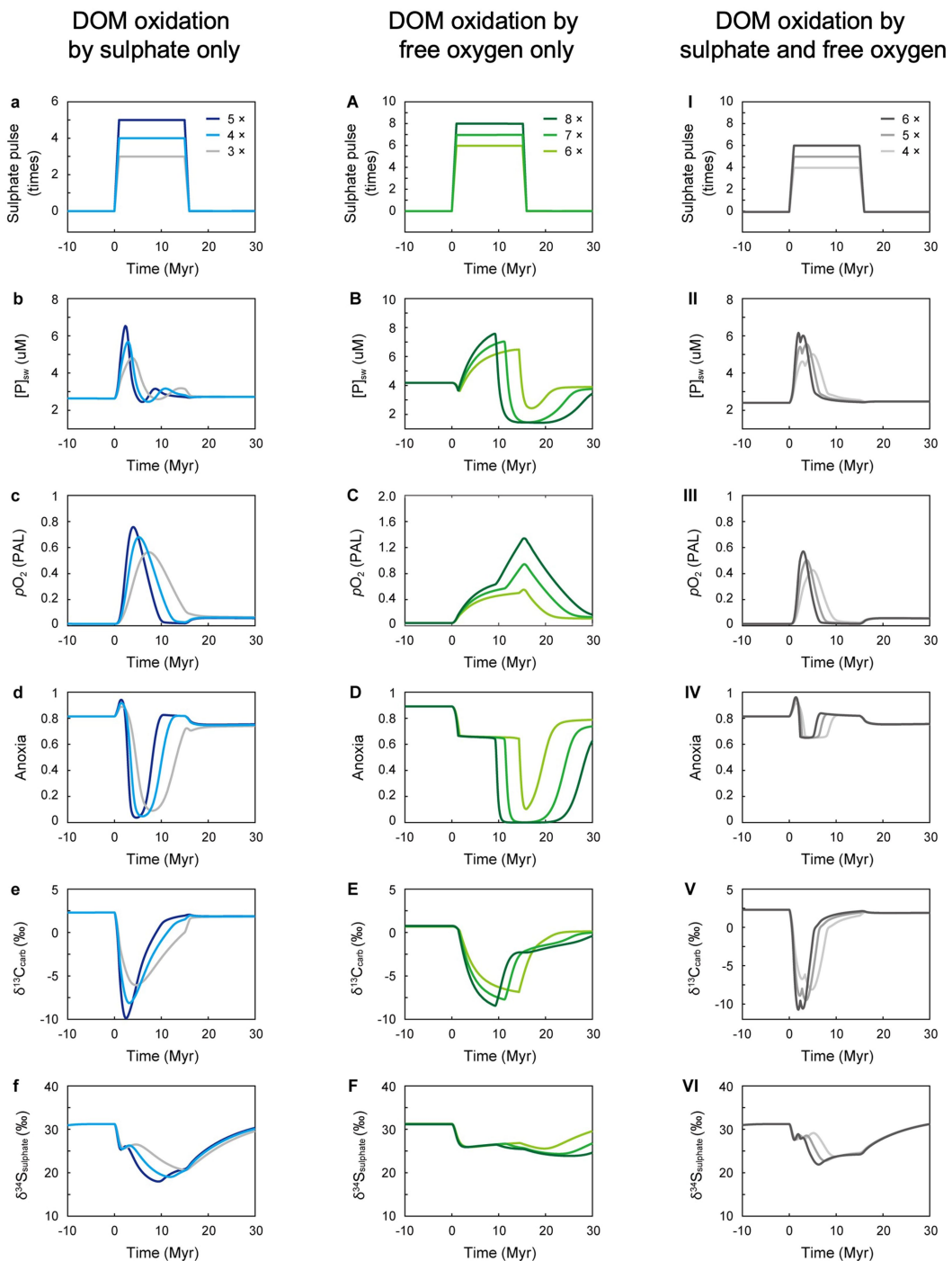
Extended Data Fig. 1 | Open-system diagenetic evolution fluid–rock interaction model. **a–c**, Fluid–rock alteration models showing the relative order of alteration for CAP, CAS, Fe, Mn, IO₃, δ¹³C, δ³⁴S_{CAS}, δ²³⁸U, δ^{44/40}Ca and ⁸⁷Sr/⁸⁶Sr. Several curves are presented for δ¹³C and δ³⁴S_{CAS} under varying DIC and sulfate concentrations in the diagenetic fluid. **d**, Fluid–rock alteration model showing the predicted trends between CAP and δ¹³C. Grey points are

CAP and δ¹³C data from all study sections. Solid and dashed lines represent different pore-water DIC concentration and δ¹³C compositions. Dotted line is trendline through data points with R value. See Supplementary Information for model description. Yellow stars mark the point at which 50% of the CAP value has been altered. Red stars mark the point at which 50% of the element of interest has been altered.



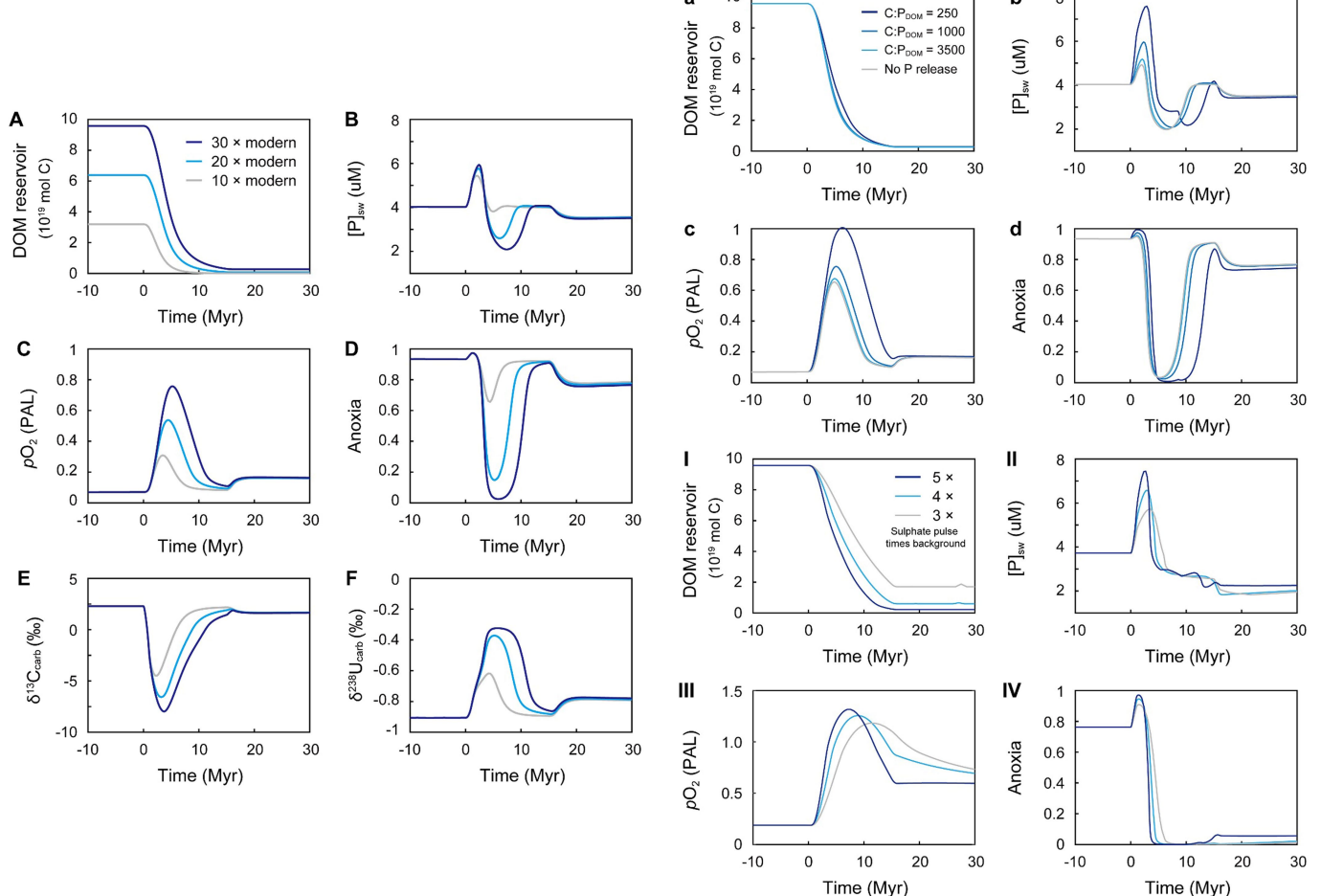
Extended Data Fig. 2 | COPSE model results comparing different hypotheses (DOM oxidation by sulfate only, elevated organic-matter recycling, elevated weathering by uplift, elevated weathering by volcanism) for the observed changes in ocean P during the SE. **a, A, I, i.** Relative increase in sulfate addition versus background flux. **b, B, II, ii.** Phosphorus concentration in seawater ($[P]_{sw}$). **c, C, III, iii.** Relative atmospheric oxygen concentration (pO_2). **d, D, IV, iv.** Degree of ocean anoxia (Anoxia). **e, E, V, v.** Modelled marine carbonate carbon-isotope composition ($\delta^{13}C_{carb}$). Note that in panel E, the $\delta^{13}C_{carb}$ reflects the $\delta^{13}C$ of pore

water DIC, not oceanic $\delta^{13}C$. **f, F, VI, vi.** Modelled marine sulfate sulfur-isotope composition ($\delta^{34}S_{sulfate}$). **g, G, VII, vii.** Modelled marine carbonate uranium-isotope composition ($\delta^{238}U_{carb}$). For the DOM oxidation hypothesis, we run the COPSE model with a DOM reservoir 30 times the size of the modern marine DIC reservoir and the C:P of the DOM reservoir is 1,000, whereas the C:P of organic matter in the organic-matter recycle model is 250 (see Supplementary Information 6 for more details). PAL, present atmospheric level.



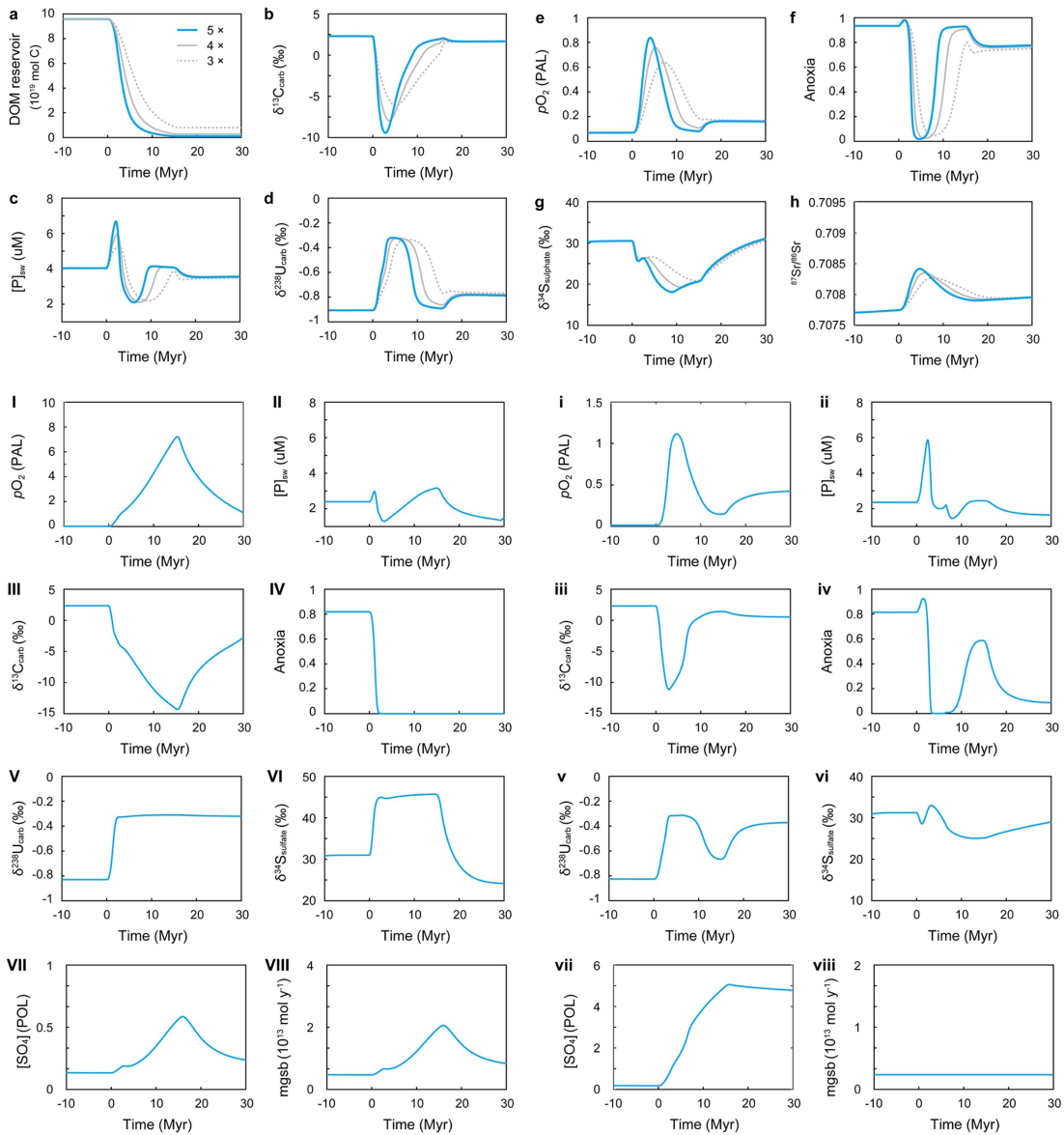
Extended Data Fig. 3 | COPSE model results comparing the oxidation of a DOM reservoir using sulfate, free oxygen (Shields et al.³⁷) and sulfate + free oxygen, respectively. **a, A, I**, Relative increase in sulfate addition versus background flux (the varying colour shades of the model lines reflect the varying magnitudes of the sulfate pulse for different model runs). **b, B, II**, Phosphorus concentration in seawater ($[P]_{sw}$). **c, C, III**, Relative atmospheric oxygen concentration (pO_2). **d, D, IV**, Degree of ocean anoxia (Anoxia). **e, E, V**, Modelled

marine carbonate carbon-isotope composition ($\delta^{13}C_{carb}$). **f, F, VI**, Modelled marine sulfate sulfur-isotope composition ($\delta^{34}S_{sulfate}$). The C:P of the DOM reservoir is set to 1,000 in all model runs. The magnitude of the sulfate pulses for each model is variable because higher additional sulfate fluxes are required for models in which DOM is oxidized by O_2 resulting from pyrite burial in comparison with models in which DOM is oxidized only by sulfate (see Supplementary Information 7 for details).



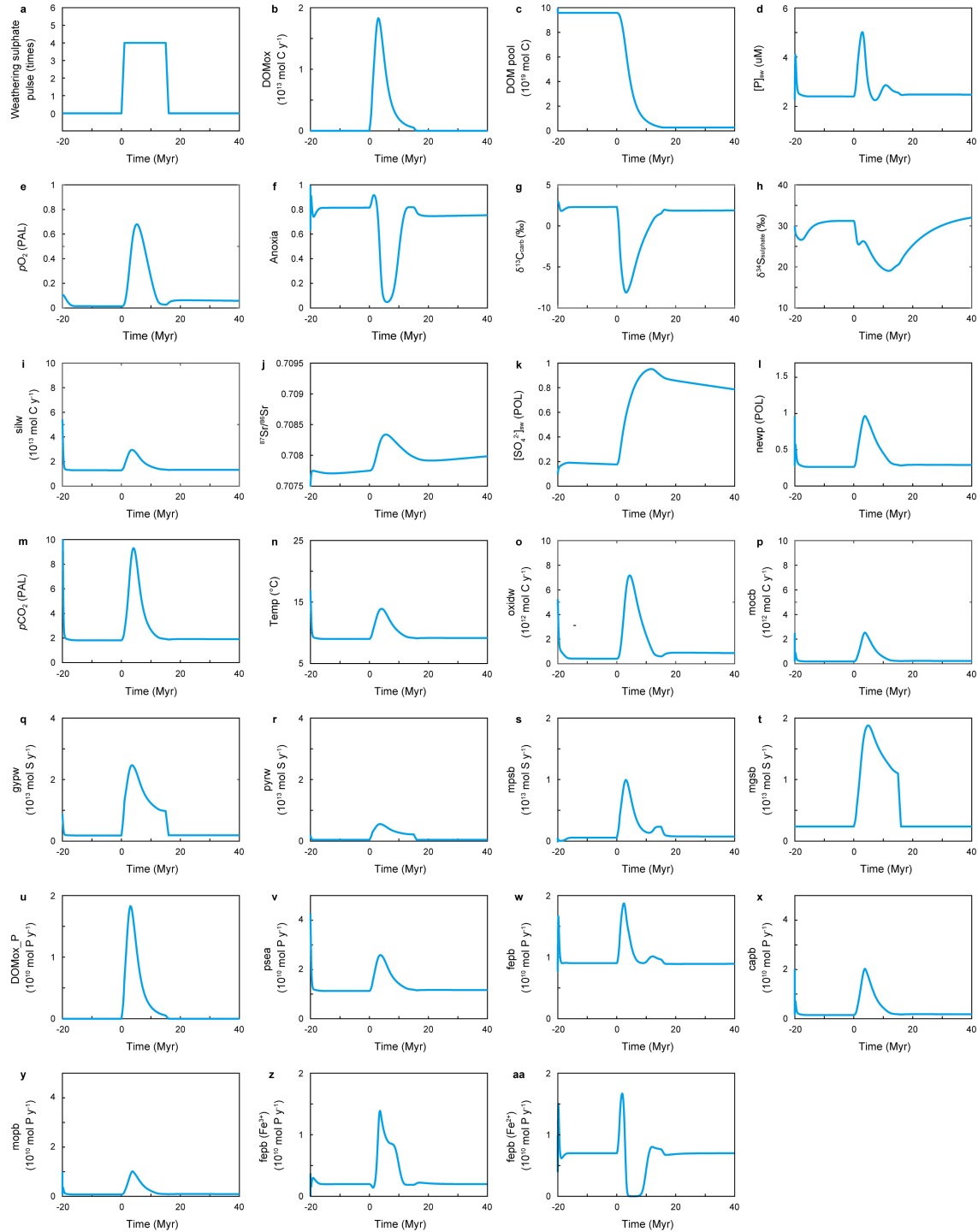
Extended Data Fig. 4 | COPSE model results with varying sizes (A–F) and variable P content (a–d) of an initial DOM reservoir and higher initial steady-state pO_2 of 20% present atmospheric level (PAL), with C:P of DOM = 250 (a–d) (no Fe²⁺-P burial) (I–IV). A, Size of DOM reservoir in moles of carbon. B, Phosphorus concentration in seawater ($[P]_{sw}$). C, Relative atmospheric oxygen concentration (pO_2). D, Degree of ocean anoxia (Anoxia). E, Modelled marine carbonate carbon-isotope composition ($\delta^{13}C_{carb}$). F, Modelled marine carbonate uranium-isotope composition ($\delta^{238}U_{carb}$). In panels A–F, we choose a sulfate pulse of four times that of the background flux and the C:P of the DOM

reservoir is 1,000. **a, I**, Size of DOM reservoir in moles of carbon. **b, II**, Phosphorus concentration in seawater ($[P]_{sw}$). **c, III**, Relative atmospheric oxygen concentration (pO_2). **d, IV**, Degree of ocean anoxia. In panels a–d, we choose a sulfate input of four times the background flux and the size of the DOM reservoir is 30 times that of the size of the modern marine DIC reservoir. For panels I–IV, the DOM reservoir is 30 times that of the size of the modern marine DIC. Higher steady-state pO_2 was achieved by adjusting the model terrestrial P-input flux and gypsum burial.



Extended Data Fig. 5 | COPSE model results varying the magnitude of a further sulfate pulse for DOM oxidation by sulfate only (no Fe^{2+} -P burial) (a–h), burying all the extra sulfate pulse as pyrite (I–VIII) and setting gypsum burial to a constant rate (i–viii). **a**, Size of DOM reservoir in moles of carbon. **b**, Modelled marine carbonate carbon-isotope composition ($\delta^{13}\text{C}_{\text{carb}}$). **c**, Phosphorus concentration in seawater ($[P]_{\text{sw}}$). **d**, Modelled marine carbonate uranium-isotope composition ($\delta^{238}\text{U}_{\text{carb}}$). **e**, Relative atmospheric oxygen concentration (pO_2). **f**, Degree of ocean anoxia. **g**, Modelled marine sulfate sulfur-isotope composition ($\delta^{34}\text{S}_{\text{sulfate}}$). **h**, Modelled marine carbonate strontium-isotope composition (${}^{87}\text{Sr}/{}^{86}\text{Sr}$). The blue line, grey line and dashed grey line are

sulfate pulses of three, four and five times the background flux, respectively. **I,i**, Relative atmospheric oxygen concentration (pO_2). **II,ii**, Phosphorus concentration in seawater ($[P]_{\text{sw}}$). **III,iii**, Modelled marine carbonate carbon-isotope composition ($\delta^{13}\text{C}_{\text{carb}}$). **VI,vi**, Evolution of ocean anoxia. **V,v**, Modelled marine carbonate uranium-isotope composition ($\delta^{238}\text{U}_{\text{carb}}$). **VI,vi**, Modelled marine sulfate sulfur-isotope composition ($\delta^{34}\text{S}_{\text{sulfate}}$). **VII,vii**, Sulfate concentration in seawater ($[SO_4]_{\text{sw}}$). **VIII,viii**, Oceanic gypsum burial rate ($mgsb$). Here we used a DOM reservoir size that is 30 times that of the size of the modern marine DIC reservoir. PAL, present atmospheric level; POL, present oceanic level.

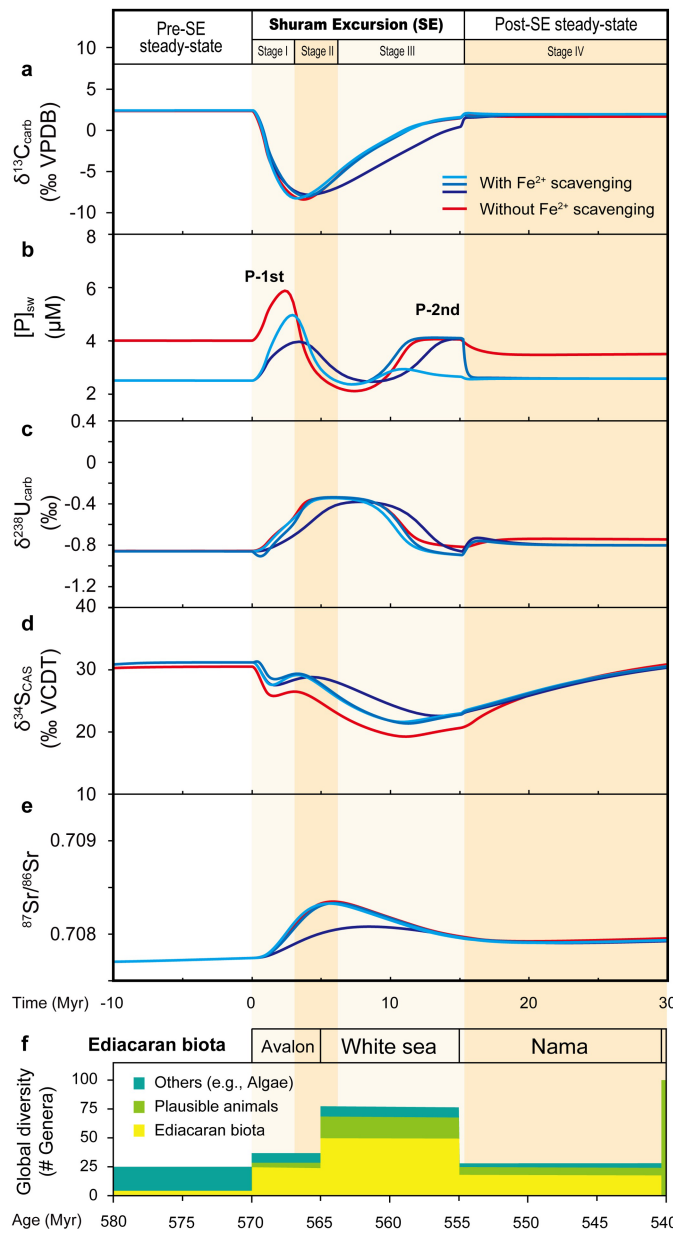


Extended Data Fig. 6 | Full COPSE model outputs for DOM oxidation by sulfate with constant Fe²⁺-bound phosphorus burial, using a sulfate pulse offour times the background flux, DOM C:P of 1,000 and the size of the DOM reservoir is 30 times the size of the modern marine DIC reservoir.

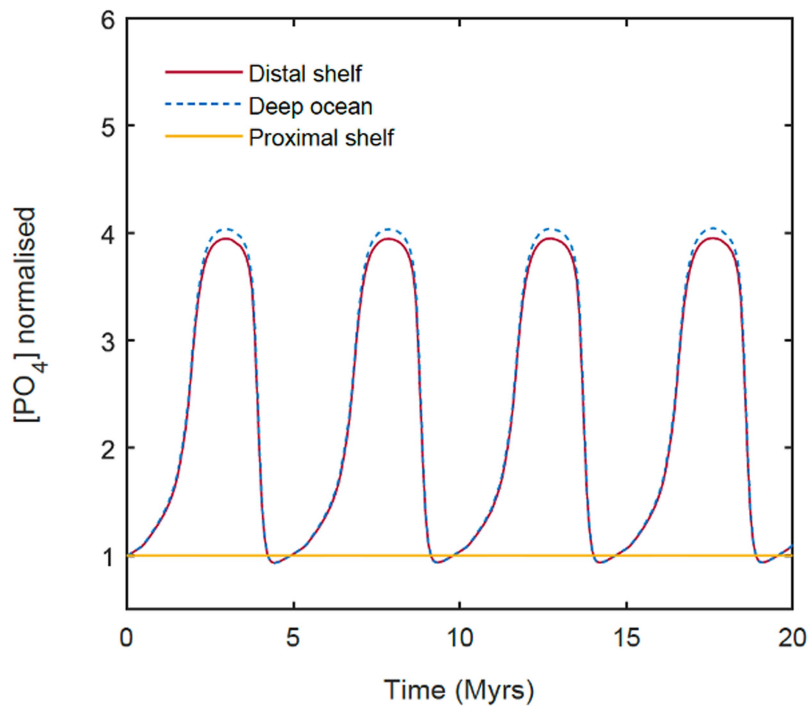
a, Weathering sulfate pulse versus background flux. **b**, DOM oxidation flux (DOM_{ox}) in moles of carbon per year. **c**, DOM reservoir (DOM_{pool}) in moles of carbon. **d**, P concentration in seawater ($[\text{P}]_{\text{sw}}$). **e**, Relative atmospheric oxygen concentration ($p\text{O}_2$) to present atmospheric level (PAL). **f**, Degree of marine anoxia (Anoxia). **g**, Modelled marine carbonate carbon-isotope composition ($\delta^{13}\text{C}_{\text{carb}}$). **h**, Modelled marine sulfate sulfur-isotope composition ($\delta^{34}\text{S}_{\text{sulfate}}$). **i**, Silicate weathering flux (silw) in moles of carbon per year. **j**, Modelled marine carbonate strontium-isotope composition ($^{87}\text{Sr}/^{86}\text{Sr}$). **k**, Relative marine sulfate concentration ($[\text{SO}_4^{2-}]_{\text{sw}}$) to present oceanic level (POL). **l**, Relative marine new primary productivity (newp) to POL. **m**, Relative atmospheric carbon dioxide

concentration ($p\text{CO}_2$) to PAL. **n**, Average global temperature (Temp) in °C. **o**, Organic carbon weathering flux (oxidw) in moles of carbon per year. **p**, Marine organic carbon burial flux (mocb) in moles of carbon. **q**, Gypsum sulfur weathering flux (gypw) in moles of sulfur. **r**, Pyrite sulfur weathering flux (pyrw) in moles of sulfur. **s**, Marine pyrite sulfur burial flux (mpsb) in moles of sulfur. **t**, Marine gypsum sulfur burial flux (mgsb) in moles of sulfur. **u**, Phosphorus releasing flux from DOM oxidation ($\text{DOM}_{\text{ox_P}}$) in moles of phosphorus. **v**, Flux of weathered phosphorus reaching the sea (psea) in moles of phosphorus. **w**, Total iron-bound phosphorus burial flux (fepb) in moles of phosphorus. **x**, Carbonate-bound phosphorus burial flux (capb) in moles of phosphorus. **y**, Marine organic phosphorus burial flux (mopb) in moles of phosphorus. **z**, Ferric iron Fe³⁺-bound phosphorus burial [fepb(Fe³⁺)] in moles of phosphorus. **aa**, Ferrous iron Fe²⁺-bound phosphorus burial [fepb(Fe²⁺)] in moles of phosphorus.

Article



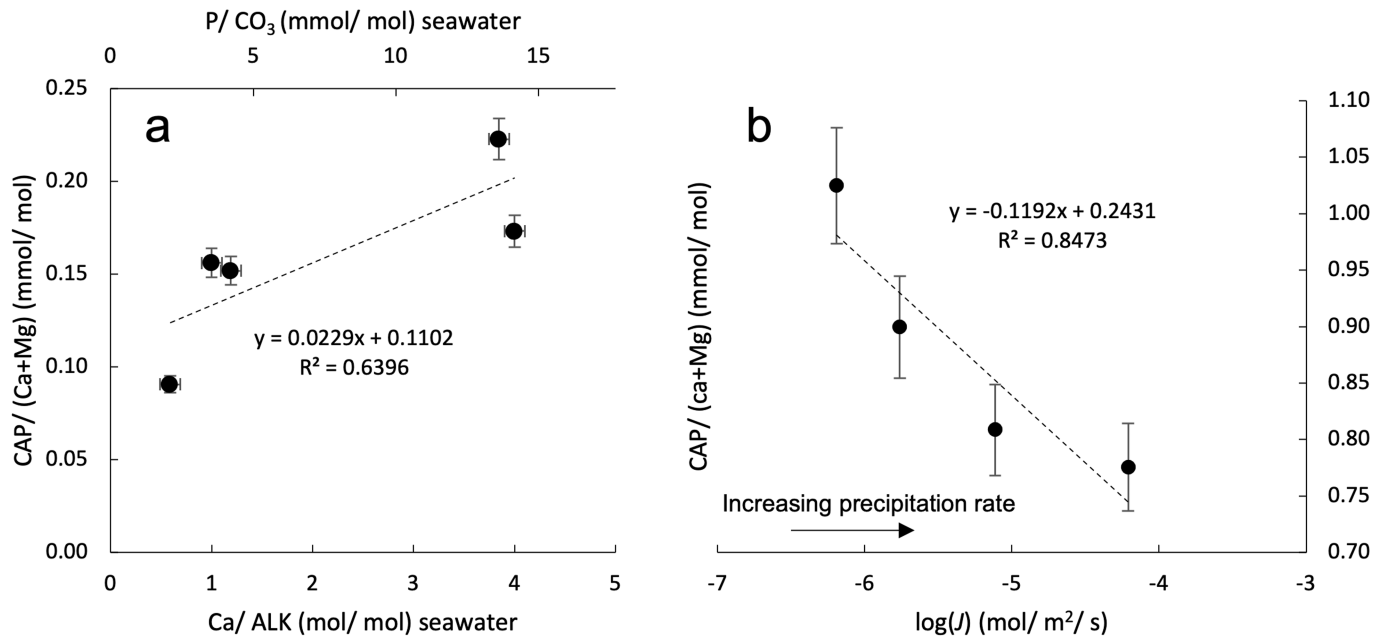
Extended Data Fig. 7 | Comparison of COPSE model results for ocean P cycling with and without P burial by Fe^{2+} scavenging. **a**, Ocean inorganic carbon isotopic composition ($\delta^{13}\text{C}_{\text{carb}}$). **b**, Ocean P concentration ($[P]_{\text{sw}}$). **c**, Ocean uranium isotopic composition recorded in carbonates ($\delta^{238}\text{U}_{\text{carb}}$). **d**, Ocean sulfur isotopic composition recorded in carbonate-associated sulfate ($\delta^{34}\text{S}_{\text{CAS}}$). **e**, Ocean strontium isotopic composition ($^{87}\text{Sr}/^{86}\text{Sr}$). **f**, Ediacaran fossil record adapted after Darroch et al.¹⁹. Stages I–IV are defined as the SE intervals of falling limb, plateau, rising limb and post-SE, respectively, as in Fig. 1, which are matched with modelled ocean P reservoir shifts. Model parameters for outputs are the same as detailed in Fig. 3 and Extended Data Fig. 6, except for the red line, which excludes P burial by Fe^{2+} scavenging (that is, a modern-style P and O_2 cycle). P-1st and P-2nd refer to CAP peaks in Fig. 1.



Extended Data Fig. 8 | Model output of a quantitative four-box ocean P cycle model. Output from Figs. 4a and 5a in Alcott et al.¹³ with the P concentrations in the respective boxes (proximal shelf, distal shelf, deep ocean) plotted. This shows the relative concentration of soluble reactive phosphorus in each ocean box during a model solution in which P levels are

oscillating on a large scale. These results show that, even under substantial changes in P concentration, the distal shelf (that is, the area of the shelf that is not dominated by riverine input) is expected to be strongly linked to the deep-ocean P concentration. See Alcott et al.¹³ for full model details.

Article



Extended Data Fig. 9 | Experimental constraints on the effects of alkalinity (a) and carbonate precipitation rate (b) on CAP values in carbonate. **a**, CAP uptake increases with progressively lower [CO₃²⁻] and alkalinity concentrations. **b**, CAP uptake decreases with increasing precipitation rate. The changes in CAP

over the observed ranges in alkalinity and precipitation rate are small compared with the effects of phosphate concentration and solution pH (Dodd et al.²⁹). All trendlines are linear fits. Error bars are $\pm 5\%$ for CAP and ± 0.1 for Ca/ALK.

Extended Data Table 1 | Statistics for CAP extraction and diagenetic measures

Section	Variables	R value	R ² value	P(α) two-tails
Parachilna Gorge (Australia)	La vs. CAP	0.46	0.21	<0.01
	Bulk rock P vs. CAP	0.37	0.14	>0.01
	TOC vs. CAP	-0.19	0.03	>0.01
	δ ¹³ C _{carb} vs. CAP	0.24	0.06	>0.01
	δ ¹⁸ O _{carb} vs. CAP	0.16	0.40	>0.01
	Mn/ Sr vs. CAP	0.17	0.17	>0.01
Cerro Rajón (Mexico)	La vs. CAP	-0.04	0.00	>0.01
	Bulk rock P vs. CAP	0.50	0.25	<0.01
	TOC vs. CAP	-0.17	0.03	>0.01
	δ ¹³ C _{carb} vs. CAP	-0.36	0.13	>0.01
	δ ¹⁸ O _{carb} vs. CAP	-0.12	0.01	>0.01
	Mn/ Sr vs. CAP	0.37	0.14	>0.01
Jiulongwan (South China)	La vs. CAP	-0.16	0.02	>0.01
	Bulk rock La vs. Bulk rock P	0.74	0.55	<0.01
	Bulk rock P vs. CAP	0.46	0.21	<0.01
	TOC vs. CAP	-0.01	0.00	>0.01
	δ ¹³ C _{carb} vs. CAP	0.24	0.06	>0.01
	δ ¹⁸ O _{carb} vs. CAP	0.40	0.16	>0.01
Death Valley (USA)	Mn/ Sr vs. CAP	0.17	0.03	>0.01
	La vs. CAP	-0.22	0.03	>0.01
	Bulk rock P vs. CAP	0.36	0.13	>0.01
	TOC vs. CAP	-0.25	0.08	>0.01
	δ ¹³ C _{carb} vs. CAP	-0.20	0.04	>0.01
	δ ¹⁸ O _{carb} vs. CAP	0.08	0.01	>0.01
Mochia-Khutuk (North-west China)	Mn/ Sr vs. CAP	0.31	0.10	>0.01
	La vs. CAP	0.14	0.02	>0.01
	TOC vs. CAP	-0.01	0.00	>0.01
	δ ¹³ C _{carb} vs. CAP	0.44	0.20	<0.01
	δ ¹⁸ O _{carb} vs. CAP	-0.26	0.07	>0.01
	Mn/ Sr vs. CAP	-0.32	0.10	<0.01
Sishang (South China)	δ ¹³ C _{carb} vs. CAP	-0.10	0.06	>0.01
	δ ¹⁸ O _{carb} vs. CAP	0.09	0.04	>0.01

The strong, statistically significant correlation between bulk-rock La and bulk-rock P in the Jiulongwan section derives from the dissolution of phosphate minerals. Yet, no statistically significant correlations are seen between La and CAP in the partial leach, implying minimal contamination from phosphate minerals for bulk-rock P. Unless otherwise stated, all elemental data are derived from CAP partial leach extraction. Isotopic data are obtained for the bulk rock. Note, when removing <10% of data points as outliers, significance levels [P(α)] increase to above 0.01 for all sections, indicating statistically insignificant correlations. All trendlines are linear fits.

Reporting Summary

Nature Portfolio wishes to improve the reproducibility of the work that we publish. This form provides structure for consistency and transparency in reporting. For further information on Nature Portfolio policies, see our [Editorial Policies](#) and the [Editorial Policy Checklist](#).

Statistics

For all statistical analyses, confirm that the following items are present in the figure legend, table legend, main text, or Methods section.

n/a Confirmed

- The exact sample size (n) for each experimental group/condition, given as a discrete number and unit of measurement
- A statement on whether measurements were taken from distinct samples or whether the same sample was measured repeatedly
- The statistical test(s) used AND whether they are one- or two-sided
Only common tests should be described solely by name; describe more complex techniques in the Methods section.
- A description of all covariates tested
- A description of any assumptions or corrections, such as tests of normality and adjustment for multiple comparisons
- A full description of the statistical parameters including central tendency (e.g. means) or other basic estimates (e.g. regression coefficient) AND variation (e.g. standard deviation) or associated estimates of uncertainty (e.g. confidence intervals)
- For null hypothesis testing, the test statistic (e.g. F , t , r) with confidence intervals, effect sizes, degrees of freedom and P value noted
Give P values as exact values whenever suitable.
- For Bayesian analysis, information on the choice of priors and Markov chain Monte Carlo settings
- For hierarchical and complex designs, identification of the appropriate level for tests and full reporting of outcomes
- Estimates of effect sizes (e.g. Cohen's d , Pearson's r), indicating how they were calculated

Our web collection on [statistics for biologists](#) contains articles on many of the points above.

Software and code

Policy information about [availability of computer code](#)

Data collection MATLAB code for COPSE is freely available at <https://github.com/sjdaines/COPSE/releases>.

Data analysis MATLAB code for COPSE is freely available at <https://github.com/sjdaines/COPSE/releases>.

For manuscripts utilizing custom algorithms or software that are central to the research but not yet described in published literature, software must be made available to editors and reviewers. We strongly encourage code deposition in a community repository (e.g. GitHub). See the Nature Portfolio [guidelines for submitting code & software](#) for further information.

Data

Policy information about [availability of data](#)

All manuscripts must include a [data availability statement](#). This statement should provide the following information, where applicable:

- Accession codes, unique identifiers, or web links for publicly available datasets
- A description of any restrictions on data availability
- For clinical datasets or third party data, please ensure that the statement adheres to our [policy](#)

All data presented in this manuscript are available from the repository link provided

Human research participants

Policy information about [studies involving human research participants](#) and [Sex and Gender in Research](#).

Reporting on sex and gender

N/A

Population characteristics

N/A

Recruitment

N/A

Ethics oversight

N/A

Note that full information on the approval of the study protocol must also be provided in the manuscript.

Field-specific reporting

Please select the one below that is the best fit for your research. If you are not sure, read the appropriate sections before making your selection.

Life sciences Behavioural & social sciences Ecological, evolutionary & environmental sciences

For a reference copy of the document with all sections, see [nature.com/documents/nr-reporting-summary-flat.pdf](#)

Ecological, evolutionary & environmental sciences study design

All studies must disclose on these points even when the disclosure is negative.

Study description

Multiple carbonate rock samples from global geological sections were processed and analysed for geochemical data. A mathematical model in Matlab was used to quantitatively explore biogeochemical feedbacks based on observed geochemical data

Research sample

Samples are carbonate rocks

Sampling strategy

Sample size was primarily based on available samples, and where available samples were taken at a density of 0.5-5m depending on section length

Data collection

Data was recorded in excel files

Timing and spatial scale

Data was collected between 12/2019 - 05/2022

Data exclusions

Outliers are left in the plots and highlighted white

Reproducibility

For every 10 samples 1 sample was measured in repeat

Randomization

N/A

Blinding

N/A

Did the study involve field work? Yes No

Field work, collection and transport

Field conditions

Field work conditions sunny, and dry

Location

See supplementary information for study site coordinates

Access & import/export

All transfer of geological samples followed national and international legislations. Where necessary permission to access land was sought and given.

Disturbance

No disturbance was caused by sticking to footpaths where possible and taking the minimum quantity of needed sample for the research work

Reporting for specific materials, systems and methods

We require information from authors about some types of materials, experimental systems and methods used in many studies. Here, indicate whether each material, system or method listed is relevant to your study. If you are not sure if a list item applies to your research, read the appropriate section before selecting a response.

Materials & experimental systems

n/a	Involved in the study
<input checked="" type="checkbox"/>	Antibodies
<input checked="" type="checkbox"/>	Eukaryotic cell lines
<input checked="" type="checkbox"/>	Palaeontology and archaeology
<input checked="" type="checkbox"/>	Animals and other organisms
<input checked="" type="checkbox"/>	Clinical data
<input checked="" type="checkbox"/>	Dual use research of concern

Methods

n/a	Involved in the study
<input checked="" type="checkbox"/>	ChIP-seq
<input checked="" type="checkbox"/>	Flow cytometry
<input checked="" type="checkbox"/>	MRI-based neuroimaging